Waveguide-Based Microscopy

Shaping a Novel Imaging Approach through Integrated Photonics

Jonas M. R. van Eeten

Delft University of Technology

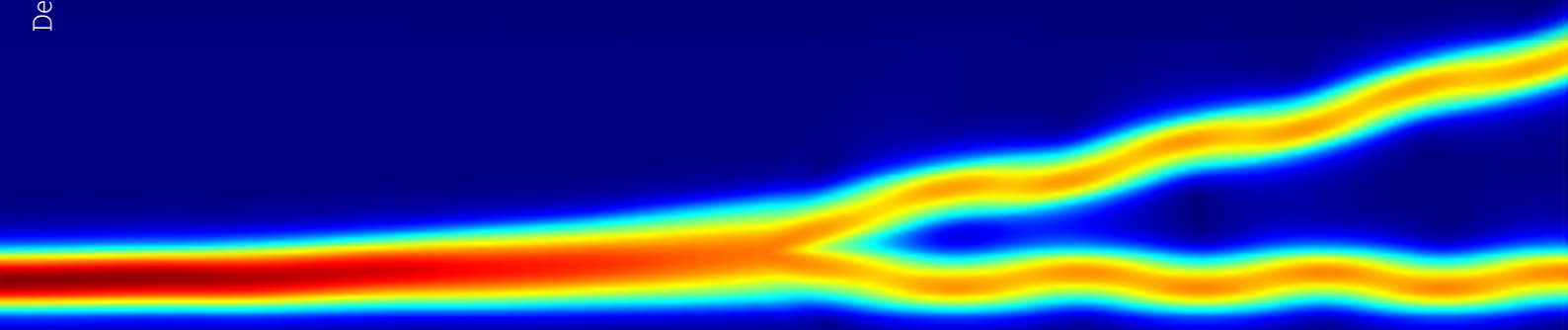

TU Delft

Waveguide-Based Microscopy

Shaping a Novel Imaging Approach through Integrated Photonics

by

Jonas M. R. van Eeten.

Submitted as part of the requirements for the degree of Master of Science in Applied Physics
To be defended publicly on Monday 22 September, 2025 at 10:00.

Student number:	4967615
Project Duration:	October 15, 2024 - September 1, 2025
Thesis Committee:	Dr. I. Esmaeil Zadeh Supervisor
	Prof. Dr. B. Rieger
	Dr. C. Errando Herranz
Department:	Imaging Physics

TU Delft

Preface

This thesis explores laboratory work, programming, simulation, theoretical analysis, and chip design within the field of optics. My interest in the subject was first sparked during my bachelor's thesis, where I was struck by the breadth of opportunities the field offers—especially when I first stepped into the laboratory to conduct my experiments. This project continues the exploration of the wide range of opportunities. At the end of this work, I shall express my gratitude to the people who supported this work.

In order to write this optics-based thesis, I had to train my patience and my love for learning. I want to share a part of a conversation of someone who had both characteristics:
After an endless powerconsuming conservation about good and evil, Eutyphroon has lost energy for some time when Socrates continued: "Then either we were wrong in our former assertion; or, if we were right then, we are wrong now." On which Eutyphroon replied:

"Indeed, one of the two must be true." Socrates continued: "Then we must start all over again and ask, What is piety? That is an enquiry which I shall never be weary of pursuing as far as in me lies; and I entreat you not to scorn me, but to apply your mind to the utmost, and tell me the truth. [...]". Eutyphroon replied: "Another time, Socrates; for I am in a hurry, and must go now." Socrates: "Alas! My companion, will you leave me in despair? I had hoped so badly to learn from you!".

Socrates continued and continued. He had patience and a love for learning. Let us go through a journey of figuring out, to our capabilities, what we may get to now about a new optical system.

Jonas M. R. van Eeten
Delft, October 2025

Abstract

Advances in compact imaging techniques continue to deliver higher resolution, lower-cost components, and increasingly miniaturized systems. Scanning Near-field Optical Microscopy (SNOM), when implemented with waveguides as scanning probes, offers a promising route toward high-resolution imaging in such platforms. The principle relies on coupling light into on-chip waveguides, which are narrow structures that guide light with high precision. After exiting the waveguide, the light reflects off the sample surface and is subsequently recaptured and guided back into the chip. The returning signal is then coupled into a separate waveguide branch. In a previously designed chip-based setup, this signal was directed into an optical fiber and detected by a photodetector, achieving a spatial resolution of $500\,\mathrm{nm}$. *By transitioning from stepwise to continuous scanning, the acquisition time was reduced by half, enabling a scan of a* 50×50 *pixel image in under* $22\,\mathrm{min}$. *An alternative approach directs the returning light through grating couplers to a camera, rather than routing it back into a fiber. This configuration supports the use of multiple waveguide probes, enabling scalable imaging. Using four probes simultaneously, a* $534\,\mu\mathrm{m}$ *wide scan clearly resolves a* $250\,\mu\mathrm{m}$ *feature, with a pixel size of* $1\,\mu\mathrm{m}$.

Contents

Nomenclature

Abbreviations

Abbreviation	Definition
APD	Avalanche PhotoDiode
DN	Digital Number
FDE	Finite-Difference Eigenmode
FDTD	Finite-Difference Time-Domain simulation method
FOV	Field Of View
GDS	Graphic Design System
GUI	Graphical User Interface
NA	Numerical Aperture
PIC	Photonic Integrated Circuit
SEM	Scanning Electron Microscope
SNOM	Scanning Near-field Optical Microscopy
SNSPD	Superconducting Nanowire Single-Photon Detector
SOI	Silicon On Insulator

Symbols

Symbol	Definition	Unit
c	speed of light in vacuum	[m/s]
f	frequency	[1/s]
k	wavevector magnitude (propagation constant)	[1/m]
m	mode/order number	[-]
n	refractive index	[-]
p	parallel polarization (TM)	[-]
r	reflection coefficient, position vector	[-],[m]
s	senkrecht polarization (TE)	[-]
t	transmission coefficent	[-]
v	phase velocity	[m/s]
x, y, z	1D position coordinates	[m]
A	area	[m^2]
B	magnetic flux density	[T]
E	electric field strength	[V/m]
F	fill factor (ratio of active to total area)	[-]
J	current density	[A/m^2]
L	Luminance	[cd/m^2]
R	reflectance, radius	[-],[m]
P	optical power	[W]
$\vec{P}$	poynting vector	[W/m^2]
T	transmittance	[-]
V	volume	[m^3]
β	propagation constant	[-]
ϵ	permittivity	[F/m]

Symbol	Definition	Unit
λ	wavelength	[m]
ϕ	phase	[rad]
ω	angular frequency	[rad/s]
θ	angle	[rad]
μ	permeability	[H/m]
Λ	grating period	[m]

1

Introduction

This chapter is organized into three sections. Section 1.1 introduces the field of integrated photonics, with a particular focus on imaging applications. Section 1.2 defines the research objective, and Section 1.3 outlines the research approach.

1.1. Imaging with Integrated Photonics

In geometrical optics, light propagates in straight lines through media such as air. To form an image, light first illuminates an object and is modified through reflection or scattering at its boundaries. Such interactions change the direction of light, as occurs with, e.g., mirrors, lenses, prisms, and crystals. By carefully shaping these optical elements, the reshaped light can be collected and directed toward a detector, enabling image formation.

This principle opened the way to non-conventional approaches in which optical functionality was transferred from bulky lenses and mirrors into compact solid-state structures, marking the birth of the field of integrated photonics [1]. Here, light no longer propagates freely through space but is confined within one or more structures of solid materials.

Unlike traditional systems, where abrupt boundaries cause sharp changes in direction, integrated photonics relies on refractive index contrasts that allow light to follow continuous, well-controlled trajectories, enabling precise steering within compact geometries. This principle can be applied in optical fibers, where light remains confined in a core and can be guided over distances or through complex paths.

An important application of integrated photonics is fiber-based microscopy. Fibers can, for example, be shaped and arranged to deliver and collect light within tissues or small structures, providing flexible imaging in hard-to-reach regions [2].

One specific approach to fiber-based imaging is scanning near-field optical microscopy (SNOM), which obtains an image by positioning a scanning fiber within the optical near-field of the surface of interest. Focusing fibers—such as tapered or lens fibers—scan the area of interest pixel by pixel to eventually form an image, a technique commonly known as *scanning near-field optical microscopy* (SNOM) [3]. This approach has the advantage of requiring relatively few components, including a photodetector and piezo-driven stages for precision positioning, which allows for simplified design and reduced costs compared to more complex lens-based systems [4].

Fig. 1.1a illustrates a lens-based approach to imaging, in which light is focused through an optical system onto a photodetector that processes the image information. Fig. 1.1b depicts the fundamental principle of SNOM-based imaging. Here, light is directed toward the surface of the imaging object in the near-field, and the reflected signal is collected to a detector. Fig. 1.1c illustrates SNOM using an optical-fiber probe: the fiber's aperture is positioned in the near-field of the sample surface, scanned point-by-point, and the transmitted or reflected light is collected by a detector [5].

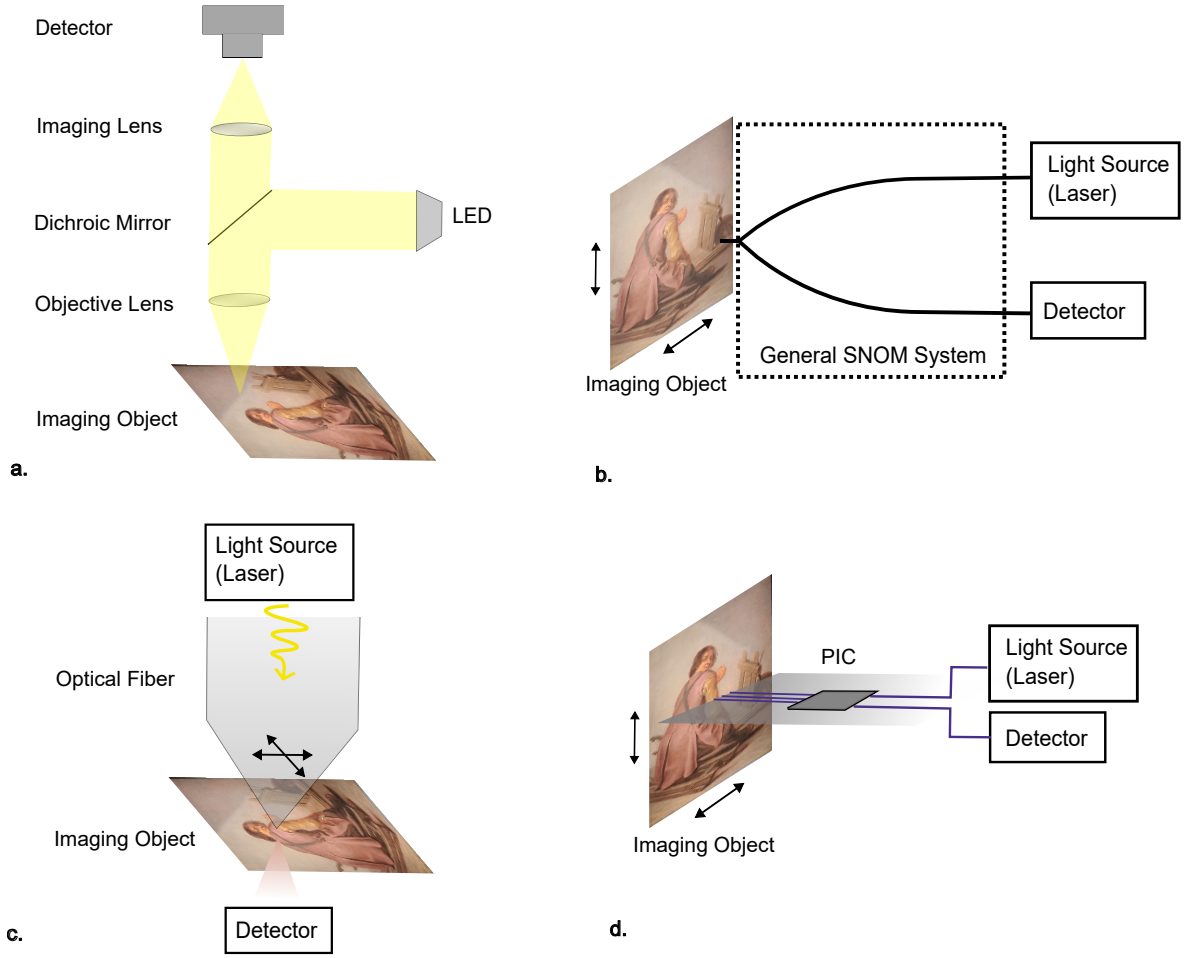

Figure 1.1: Schematic comparison of (a) a conventional imaging system, (b) a scanning near-field optical microscopy (SNOM) setup, (c) SNOM with a tapered fiber probe, and (d) scalable SNOM using a photonic integrated circuit (PIC). Background image adapted from *Portret van een zittende man op een kruiwagen* (ca. 1630, Jacob Jansz. van Velsen, Museum Prinsenhof Delft).

The main motivation for using a scanning probe is that it allows spatial resolution beyond the conventional diffraction limit of far-field optics, which normally restricts the smallest resolvable features to roughly half the wavelength of light. For example, a conventional microscope lens system (Fig. 1.1a) is constrained by diffraction and the finite size of the lenses, and is said to operate in the far-field. A more detailed theoretical discussion of the diffraction limit is given in section 2.4.

In contrast, a scanning near-field optical microscopy (SNOM) setup (Fig. 1.1b) delivers light through a probe that scans in close proximity to the sample surface, eliminating the reliance on lenses. Because the light–sample interaction occurs locally—before diffraction takes effect—SNOM enables imaging with subwavelength resolution. The ultimate resolution is mainly determined by the probe's optical spot size as well as its scanning step size.

Despite their widespread use, optical fibers present significant limitations. With a typical cladding diameter of $125, \mu$m [6], optical fibers remain relatively bulky and are not well suited for large-scale integration. Raster scanning with fibers is particularly time-consuming because the light must be guided sequentially across the image, forming each pixel one at a time. A natural next step is to replace fibers with fully integrated circuits on a single chip, paving the way for scalable and miniaturized optical systems. Such on-chip photonics are commonly referred to as Photonic Integrated Circuits (PICs).

Fig. 1.1d shows SNOM implemented on a photonic integrated circuit. In this arrangement, light is guided through integrated waveguides or branches, and multiple output or collection paths can be

combined to enable parallel detection and faster image formation. As in conventional SNOM, the near-field interaction requires that the guiding or collecting structures be positioned in close proximity to the sample surface to capture evanescent fields.

In addition to their compactness and scalability, photonic integrated circuits offer advantages in cost-effectiveness and reliability [7–9]. Analogous to how electronic integrated circuits revolutionized electronics, PICs integrate multiple optical functions onto a single chip. By replacing electrical interconnects with optical links, they can significantly reduce power consumption, which is a key reason why PICs are increasingly deployed in data-center interconnects to accommodate the rapid growth of internet traffic [10].

Beyond telecommunications, PICs finds applications in diverse fields, including LiDAR sensing, biosensing, and quantum computing and communication. [11–13]

Previous studies have already successfully utilized photonic integrated circuits in imaging, particularly for biological applications, employing fluorescence-based microscopy techniques. These techniques rely on single-molecule localization and fluorescence excitation, which provide molecular specificity and high contrast, enabling the visualization of intracellular structures beyond the diffraction limit [14–16]. The need for fluorescence arises from its ability to selectively label structures, allowing researchers to track individual molecules and achieve super-resolution imaging. However, fluorescence microscopy often requires complex sample preparation, photostable dyes, and suffers from photobleaching, which can limit long-term observations [14, 17].

In addition, recent studies have extended PIC-based microscopy to both biological and non-biological microscopy without relying on fluorescence, using waveguides as the illumination source [18–20]. However, component-based raster-scan super-resolution approaches have rarely been applied to non-biological samples, leaving a gap that this work aims to address.

Therefore, in this work, SNOM using PICs is performed on non-biological, solid-state materials. These samples are chosen for practical reasons: they are stable, allowing long acquisition times without motion artifacts, and they do not require fluorescent labeling or other contrast agents. This choice enables a clear demonstration of the capabilities of PIC/waveguide-based scanning microscopy.

1.2. Research Objective

The objective of this research is to obtain a quantitative understanding of the capabilities and limitations of near-field, PIC-based microscopy in the context of industrial applications. Accordingly, the central research question is formulated as follows:

What technical challenges limit the performance of photonic waveguide-based imaging systems, and how can they be addressed to achieve more stable and higher-quality images?

To address this central question, the objective can be divided into several sub-questions:

1. How to stabilize the system, enabling it to give more noise-free and consistent results.
2. What PIC–sample configurations are effective for fast an continuous image formation?
3. Which sample structures and materials are best suited for scanning with PIC-based systems?
4. What strategies can be used to accelerate the rather slow scanning process?

1.3. Research Approach

The research approach focuses on improving the current experimental setup and exploring the capabilities of near-field PIC-based imaging. The key steps are:

1. *Initial Reproduction and Setup Validation:* Image measurements will be performed with the existing setup. To address challenges in coupling and positioning, the aim is to establish a reliable method for obtaining high-quality images. A repeatable alignment protocol will be developed to ensure consistent experimental conditions.

2. *Development of a Fast Scanning Method:* The custom MATLAB graphical interface controlling the scanning process will be rewritten to enable continuous instead of stepwise scanning. This system will then be calibrated and tested.
3. *Sample Design for Testing:* New imaging samples will be designed for scanning by generating `.gds` (Graphic Data System) files in Python.
4. *Iterative Optimization:* Once the scanning pipeline is in place, the setup will undergo iterative testing. Noise sources (optical, mechanical, thermal) will be identified experimentally and reduced through mechanical stabilization, shielding, or component replacement. Simulations shall be carried out to find for potential optimizations as well.
5. *Scaling Up the Probe Array:* In later stages, the project will focus on scaling from single-waveguide scanning to multi-probe operation. The feasibility of parallel scanning will be explored by designing new PICs with multiple outputs or more complex routing schemes.
6. *Data Handling and Visualization:* Scan data will be analyzed in terms of resolution and contrast. Post-processing will be applied where necessary to remove artefacts and to quantify spatial resolution.

This approach enables iterative system development through continuous feedback between design, measurement, and analysis. Key technical skills developed in the project include designing photonic structures in `GDS` format, implementing object-oriented system control via a custom MATLAB GUI, and performing optical simulations to guide design decisions.

When it comes to lab work, the primary focus is systematically addressing practical challenges as they arise—such as optical noise, mechanical misalignment, and resolution constraints.

2

Theoretical Background

To understand how waveguide-based imaging operates and how it can be optimized, it is essential to analyze the underlying physical processes. Section 2.1 introduces different models describing the behavior of light, followed by Section 2.2, which outlines how light interacts with matter to generate image information. Section 2.3 examines mode profiles, describing the electromagnetic field distribution in optical fibers and waveguides. The resolution limit is addressed in Section 2.4, while Section 2.5 explains the working principle of grating couplers. Finally, Section 2.6 discusses noise originating from Fabry-Pérot interferometry.

2.1. Models of Light

When analyzing the optical phenomena relevant to this work, it is essential to consider two different models used to describe light, each offering unique insights depending on the context.

One of the most fundamental representations is the *ray model*, which treats light as straight-line rays traveling in a straight line from point A to point B in space. This model forms the basis of *geometric optics* and is especially useful for understanding macroscopic systems involving lenses, mirrors, and imaging geometries.[21]

A classic example demonstrating the utility, and showing the concept of the ray model is the *pinhole camera*. In this setup, light rays from different points on an object pass through a small aperture and project onto an image plane. Since the rays propagate in straight lines, light from the top of the object reaches the bottom of the image plane, and vice versa—producing an *inverted image*. This inversion directly illustrates the ray-like propagation of light.

Secondly, light should be treated as a wave, a propagating oscillation of physical quantities such as amplitude and phase over space and time. This wave model is essential for describing phenomena like interference, diffraction, and polarization. A classical demonstration of this behavior is Young's double-slit experiment. In this setup, an opaque screen with two narrow, parallel slits allows light to pass through and illuminate a detection screen behind it. The resulting pattern of alternating bright and dark fringes arises from the superposition of the wavefronts emerging from each slit, exhibiting constructive and destructive interference. When capturing light intensities in an imaging system like in this project, these interference effects needs to be taken into account. More details about this are given in section 2.4.

These wave phenomena can be fully described by treating light as a time-varying electromagnetic field governed by Maxwell's equations. These fundamental equations relate the spatial and temporal evolution of the electric field $\vec{E}$ and magnetic field $\vec{B}$, and fully describe how light propagates, reflects, refracts, or interacts with materials—whether dielectric, metallic, or absorbing. This formulation allows for more detailed modeling of how light behaves at material boundaries. Modern optical simulation tools—such as finite-difference time-domain (FDTD) and finite element method (FEM) solvers—are

commonly used to numerically solve Maxwell's equations (eq. 2.1) for complex photonic structures. These methods are particularly useful for analyzing integrated photonic systems.

2.2. Light-Matter Interaction

In an optical imaging system, understanding the interaction between light and materials is essential for accurately capturing image information. This is particularly important in photonic integrated surfaces, where the optical properties of the materials play a critical role. When light strikes a surface, it may be partially reflected, transmitted (i.e., refracted), absorbed, or scattered. The phenomena can be described by Maxwell's equations. Their derivation is not included here, but can be found, for example, in Griffiths, *Introduction to Electrodynamics* [22]. These equations are:

$$\begin{aligned} \nabla \cdot \vec{E} &= \frac{\rho}{\epsilon_0}, && \text{(Electric Gauss's law)} \\ \nabla \cdot \vec{B} &= 0, && \text{(Magnetic Gauss's law)} \\ \nabla \times \vec{E} &= -\frac{\partial \vec{B}}{\partial t}, && \text{(Faraday's law of induction)} \\ \nabla \times \vec{B} &= \mu\epsilon\frac{\partial \vec{E}}{\partial t} + \mu\vec{J}, && \text{(Ampère-Maxwell law)} \end{aligned} \tag{2.1}$$

where $\vec{E}$ and $\vec{B}$ are the electric and magnetic fields, ρ is the charge density, $\vec{J}$ the current density, and ϵ and μ the permittivity and permeability, respectively.

Another fundamental equation is the wave equation for a homogeneous, linear, isotropic medium:

$$v^2(\vec{r})\nabla^2\vec{E}(\vec{r},t) = \frac{\partial^2\vec{E}(\vec{r},t)}{\partial t^2}. \tag{2.2}$$

with phase velocity $v = \frac{1}{\sqrt{\mu\epsilon}} = \frac{c}{n}$.

2.2.1. Reflection and Transmission

Key relations governing light–matter interaction, based on the lecture notes of Konijnenberg [23], are summarized here.

To describe reflection and transmission, Eq. (2.2) can be solved to obtain a plane-wave solution:

$$\vec{E}(\vec{r},t) = \vec{E}_0\, e^{i(\vec{k}\cdot\vec{r}-\omega t)}, \qquad |\vec{k}| = \frac{n\omega}{c}. \tag{2.3}$$

Here, $\vec{E}_0$ represents the (complex) amplitude, $\vec{k}$ the wavevector, n the refractive index, ω the angular frequency, and $\vec{r}$ the position vector. This form describes the propagation of the electric field. Substituting this solution into Faraday's law (Eq. 2.1) gives the corresponding magnetic field:

$$\vec{B}(\vec{r},t) = \frac{1}{\omega}\,(\vec{k}\times\vec{E}_0)\, e^{i(\vec{k}\cdot\vec{r}-\omega t)}. \tag{2.4}$$

Using the relation $|\vec{k}|/\omega = 1/c$, this shows that the magnetic field is perpendicular to both the propagation direction and the electric field:

$$\vec{B} = \frac{n}{c}\,\hat{k}\times\vec{E}. \tag{2.5}$$

The propagation direction of light is defined to be along the wavevector $\vec{k}$. Its unit vector can be denoted as $\hat{k}$. The *polarization* of light can be described as the direction of oscillation of the electric field $\vec{E}$ and therefore fixes the magnetic field $\vec{B}$ as well. Two types of polarization are important when describing light propagating towards a surface as a combination of the two can make up any polarization:

- **TE-polarization / s-polarization**: The electric field **E** is parallel to the surface. TE stands for Transverse Electric, and s for the German word for perpendicular 'senkrecht'.
- **TM-polarization / p-polarization**: The magnetic field **B** is parallel to the surface. As TM stands for transverse magnetic and p for parallel.

The polarization of light plays an important role in determining how much of it is reflected or transmitted at an interface between two media. Consider a plane wave incident from a first medium with refractive index n_1 onto the second medium with refractive index n_2.

The component of the electric field is continuous across the surface of the two media. By taking the integral form of Faraday's law across an infinitely thin surface over this boundary region:

$$\begin{aligned}
\nabla \times \vec{E} &= -\frac{\partial \vec{B}}{\partial t} \\
\int_{x_1}^{x_2} \vec{E} \cdot ds &= -\int \frac{\partial \vec{B}}{\partial t} \cdot \hat{n} dA \\
\vec{E}(x_2) - \vec{E}(x_1) &= 0 \\
\vec{E}(x_1) &= \vec{E}(x_2)
\end{aligned} \tag{2.6}$$

The same boundary condition applies to the magnetic field $\vec{B}$. This can be seen by considering the analogously structured Ampère–Maxwell law:

$$\nabla \times \vec{B} = \mu\epsilon \left(\frac{\partial \vec{E}}{\partial t} + \vec{J} \right),$$

and setting the current density $\vec{J} = 0$. Applying this boundary condition to the case of an incident electromagnetic wave, one obtains:

$$E_{i//} + E_{r//} = E_{t//}, \quad B_{i||} + B_{r//} = B_{t//}. \tag{2.7}$$

Thus, these fields are continuous across the tangential components at the interface. Next, by applying Eq. 2.4 and evaluating the cross product, one obtains the result for TE polarization:

$$\begin{aligned}
E_i + E_r &= E_t && \text{Continuity of } E_{\|} \\
n_1 E_i \cos\theta_i - n_1 E_r \cos\theta_i &= n_2 E_t \cos\theta_t && \text{Continuity of } B_{\|},
\end{aligned}$$

where θ_i is the angle in incidence relative to the normal of the interface. The angle of transmission into the second medium is denoted by θ_t.

Rearranging these equation lead to the Fresnel equation for TE-polarization, or s-polarization:

$$r_s = \frac{n_1 \cos\theta_i - n_2 \cos\theta_t}{n_1 \cos\theta_i + n_2 \cos\theta_t}, \quad t_s = \frac{n_2 \cos\theta_i - n_1 \cos\theta_t}{n_2 \cos\theta_i + n_1 \cos\theta_t}, \tag{2.8}$$

where $r_s = |E_r/E_i|_s$ and $r_p = |E_r/E_i|_p$ are the reflection coefficient for s- and p-polarized light respectively.

Similarly for p-polarization:

$$\begin{aligned}
E_i \cos\theta_i - E_r \cos\theta_i &= E_t \cos\theta_t && \text{Continuity of } E_{\|} \\
n_1 E_i + n_1 E_r &= n_2 E_t && \text{Continuity of } B_{\|},
\end{aligned}$$

which is solved by

$$r_p = \frac{n_2 \cos\theta_i - n_1 \cos\theta_t}{n_2 \cos\theta_i + n_1 \cos\theta_t},$$
$$t_p = \frac{2n_1 \cos\theta_i}{n_2 \cos\theta_i + n_1 \cos\theta_t}.$$

From here, the *reflectance* R (i.e., the ratio of reflected power to incident power) is obtained by taking the magnitude squared of the reflection coefficients:

$$R_s = |r_s|^2, \quad R_p = |r_p|^2. \tag{2.9}$$

Similarly, the transmittance T is defined as the fraction of power transmitted across the boundary and, for non-absorbing media, satisfies:

$$R + T = 1. \tag{2.10}$$

Higher reflectance, and consequently lower transmittance, results in more light being redirected toward the detector, producing brighter image regions. In microscopy techniques under development, it is desirable for the reflectance (R) and transmittance (T) to differ as much as possible between materials in order to enhance contrast and enable reliable material discrimination.

2.2.2. Absorption

In optically absorbing materials, part of the light energy can be transferred to the material—e.g. as heat—resulting in a loss of optical power. This loss due to *absorption* depends on several factors: the path length x through the material, the molar concentration c (in mol/L) of absorbing species, and the absorption coefficient α, which varies with both the material and the wavelength of the incident light [24].

These dependencies combine into the following differential form:

$$dI = -\alpha c I \, dx \tag{2.11}$$

where I is the light intensity at position x, dx is an infinitesimal path length, c is the molar concentration of the absorbing species, and α is the absorption coefficient.

Solving this equation over a path length l leads to Beer's law, which describes the exponential decay of light intensity due to absorption. Here, the photon is absorbed into thermal energy.

$$I = I_0 \exp(-\alpha c l) \tag{2.12}$$

Here, I_0 is the incident intensity at the entrance of the medium, and I is the remaining intensity after propagating through a thickness l.

Absorption occurs when the energy of an incoming photon matches the energy difference between two electronic states of an atom or molecule. In this process, an electron is excited to a higher energy level. Instead of re-emitting the photon, the absorbed energy is typically converted into heat, as it is quickly dissipated through interactions with the surrounding material. This process is commonly referred to as *dissipative absorption* [25].

In the context of this project, absorption contributes to propagation losses within optical waveguides, reducing the amount of light that reaches the sample. In microscopy, absorption can also influence image contrast, depending on the material under investigation.

2.2.3. Scattering

When light illuminates a surface, atoms or molecules interact with the electromagnetic field and re-radiate it in various directions. Each atom behaves like an oscillating dipole, scattering the incident light. There are two main types of scattering.

If the photon energy is too low to excite an electronic transition in the sample, the oscillating charges re-emit light at the same frequency as the incident light, redirected in many directions. This is called *non-resonant scattering*.
If the photon energy matches an electronic or collective excitation, *resonant scattering* occurs. The dominant type depends on the photon energy relative to the material's electronic structure [25].

Therefore, to minimize scattering in waveguide-based microscopy, one should ensure smooth surfaces, proper alignment of the probe, and avoid photon energies that induce resonant interactions.

2.3. Mode Profiles

To effectively guide and manipulate light in integrated photonic circuits, it is essential to understand the spatial distribution of the electromagnetic field inside optical waveguides and fibers. This section provides an overview of the underlying theory of mode profiles, following the treatment in Hunsperger's *Integrated Optics: Theory and Technology* [7].

A waveguide is a fundamental component of integrated photonic circuits. Its main characteristic is that the electric field maintains a constant distribution along its entire length. In other words, the field profile remains the same at any cross-section (see Fig. 2.1). The field in a waveguide could be thought of as a uniform plane, propagating along one direction, say along the z-axis. This uniformity is achieved by carefully selecting the materials surrounding the waveguide. A common type is the buried channel waveguide, where the guiding core has a beam-like shape and is embedded in a cladding with a lower refractive index. Waveguides are used as interconnecting circuit elements in PIC devices.

In a waveguide, only a limited number of field distributions can exist, known as modes. These arise from the restricted set of solutions to the wave equation for the electric field (Eq. 2.2). The velocity is given by $v(\vec{r}) = c/n(x, y)$, where the refractive index $n(x, y)$ varies between the waveguide core and the surrounding cladding.

Since the waveguide is translationally invariant along the z-axis, a natural solution is a field propagating in the z-direction as a plane wave, modulated by a transverse mode profile. The time-harmonic solution can therefore be written as

$$\vec{E}(\vec{r}, t) = \vec{E}(x, y)\, e^{i(\omega t - \beta z)}, \tag{2.13}$$

where $\omega = kc$ is the angular frequency in vacuum, and β is the propagation constant along z (i.e. $\beta = k_z$).

For a monochromatic wave, consider only the spatial part of the solution: $\vec{E}(\vec{r}) = \vec{E}(x, y)e^{-i\beta z}$. Substituting this into the wave equation 2.2 and separating variables leads to the scalar wave equation in the transverse plane:

$$\frac{\partial^2 \vec{E}}{\partial x^2} + \frac{\partial^2 \vec{E}}{\partial y^2} + \left[k^2 n^2(x, y) - \beta^2\right] \vec{E}(x, y) = 0. \tag{2.14}$$

Solving equation 2.14 for a given refractive index distribution $n(x, y)$ yields the allowed mode profiles $\vec{E}(x, y)$ and their corresponding propagation constants β. Because the refractive index differs between the waveguide core and cladding, different field equations apply in each region. For example, when considering transverse electric (TE) modes—where the electric field is polarized along y and has no z-component—solving the wave equation in the x-direction gives separate equations in the core and cladding:

$$\partial^2/\partial x^2 \vec{E}(x,y) + (k^2 n_1^2 - \beta^2)E(x,y) = 0$$
$$\partial^2/\partial x^2 \vec{E}(x,y) + (k^2 n_2^2 - \beta^2)E(x,y) = 0$$

Applying boundary conditions—requiring continuity of both $\vec{E}(x,y)$ and its derivative $\partial\vec{E}(x,y)/\partial x$ at the interfaces—leads to sinusoidal solutions in the core and exponential decay in the cladding. These solutions are known as modes. The first three TE mode are illustrated in Fig. 2.1. A waveguide is said to be *single-mode* when it supports only the fundamental spatial mode for a given wavelength and polarization.

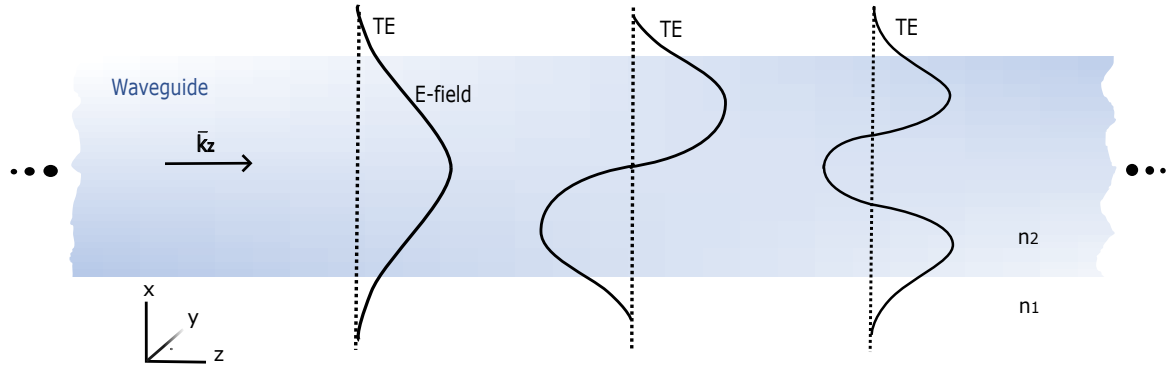

Figure 2.1: Some solutions to the wave equation for TE polarization within a waveguide. The modes are continuous at the interface between materials with refractive indices n_1 and n_2.

In practical photonic structures, additional losses can arise when the spatial profile of a guided mode in one section of the waveguide does not perfectly match the mode in the next section, or when light leaks out of the guided region into the surrounding medium. These effects, which reduce transmission efficiency, are captured by two main mechanisms: *mode mismatch loss* and *radiation loss*.

Mode mismatch loss arises when optical modes do not align properly at an interface between two waveguide sections. This situation can occur, for example, at a sudden change in width, height, or geometry, which prevents perfect coupling of the fields. As a result, part of the optical power is scattered or reflected, lowering the transmission efficiency of the device.

Radiation loss occurs when guided light is no longer fully confined within the waveguide. This happens when energy leaks into the surrounding medium or into unguided modes. A common case is *bending loss*, where tight waveguide curvature forces part of the optical field outside the core. Such radiation not only reduces the transmitted signal but can also limit the integration density of photonic circuits, since minimum bend radii must be respected.

Therefore, studying the optimal shape of waveguide bends is essential to minimize these losses and maximize signal-to-noise ratio. Within this project, the study of waveguide width transitions and Y-splitting structures serves as a relevant example where both types of losses need to be considered. [7]

2.4. Resolution Limit

In microscopy, *resolution* is a key concept. It describes the minimum distance between two neighboring points on an object that can still be distinguished as separate, typically expressed in nanometers. A useful analogy is comparing two televisions of the same size: a higher pixel count allows finer detail, although this says little about the correctness of the pixel values themselves.

It is important to distinguish spatial resolution from accuracy, since an image may appear sharp while still misrepresenting intensity or color information. A practical way to assess resolution is to examine a well-defined edge in the image and measure the physical distance over which the intensity transitions from one level to another (the width of the “ramp”) [26].

Researchers aim to resolve ever smaller features. However, the wave nature of light imposes a fundamental constraint—the *diffraction limit*—which bounds the resolution achievable with conventional optical systems.

A useful way to illustrate this limitation is by considering light incident on a diffraction grating, where the periodic trenches represent the smallest features to be distinguished. When a plane wave with wave vector k impinges on the grating, the periodic structure causes the light to be scattered into discrete *diffraction orders*, indexed by m, see Figure 2.2. Each diffraction order propagates at an angle θ_m relative to the grating normal. The angles are determined by the grating equation

$$\Lambda \sin\theta_m = m\lambda_n, \tag{2.15}$$

where Λ is the grating period, m is an integer (positive, negative, or zero) denoting the diffraction order, and λ_n is the wavelength of the incident light in a medium with refractive index n. The wavelength in the medium is related to the free-space wavelength λ_0 by $\lambda_n = \lambda_0/n$, which can be used as a convenient substitution.

The $m = 0$ diffraction order corresponds to the undiffracted beam and exists for any grating period Λ. To extract spatial information from the grating, at least the ± 1 diffraction orders must be collected by the imaging system. The minimum numerical aperture (NA) required for this is given by

$$NA \equiv \sin\theta_1^{\min} = \frac{\lambda_n}{\Lambda}. \tag{2.16}$$

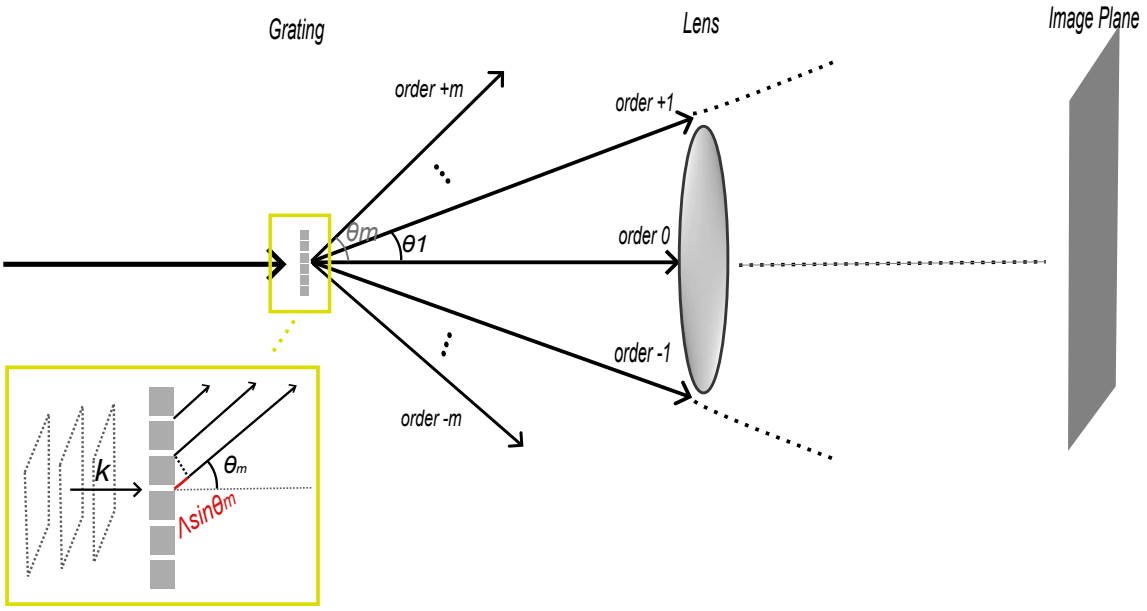

Figure 2.2: Schematic illustration of diffraction from a periodic grating. To resolve the grating structure, the imaging lens must capture at least the ± 1 diffraction orders in addition to the $m = 0$ order. In the configuration shown, these orders miss the lens and therefore do not reach the image plane, preventing the grating period Λ from being determined using $\Lambda \sin\theta_m = m\lambda$.

To investigate ways to overcome the diffraction limit, consider an incident plane wave propagating from medium 1 into medium 2. Let $\vec{r} = (x, y, z)$ denote a position in space, and choose coordinates such that the plane of incidence lies in the x–z plane, with x oriented along the interface and z perpendicular to it. The plane wave can then be expressed as

$$\vec{E}(\vec{r}, t) = \vec{E}_0\, e^{i(\vec{k}\cdot\vec{r} - \omega t)} = \vec{E}_0\, e^{i(k_x x + k_y y + k_z z - \omega t)}. \tag{2.17}$$

The *dispersion relation* describes how the wavevector relates to the frequency of a wave. Since the plane of incidence is chosen to lie in the x–z plane, the y-component vanishes ($k_y = 0$), and the relation for a monochromatic plane wave in a homogeneous medium of refractive index n is

$$|k|^2 = k_x^2 + k_z^2 = \left(\frac{2\pi n}{\lambda_0}\right)^2, \tag{2.18}$$

where λ_0 is the free-space wavelength, and k_x and k_z are the wave vector components parallel and perpendicular to the interface, respectively. At the interface between two media, k_x must be conserved (boundary condition from translational symmetry along x). Consider the case where the incident wave satisfies

$$k_x > \frac{2\pi n_r}{\lambda_0}, \tag{2.19}$$

Here, n_r is the refractive index of the second medium into which the light is refracted. Substituting this into the dispersion relation gives

$$k_z^2 = \left(\frac{2\pi n_r}{\lambda_0}\right)^2 - k_x^2. \tag{2.20}$$

This equation can become negative as $k_x^2 > \left(\frac{2\pi n_r}{\lambda_0}\right)^2$. Then k_z^2 is less than zero, which means that k_z is purely imaginary. So the field in the second medium becomes

$$E(x,z) = E_0 e^{i(k_x x + i|k_z|z)} = E_0 e^{ik_x x} e^{-|k_z|z} \tag{2.21}$$

This corresponds to a wave that travels along the surface (x) while its amplitude decays exponentially in the direction perpendicular to the surface between the two media (z), forming a highly localized evanescent field [23].

Because the field decays within a very short distance from the surface, the light remains confined close to the originating structure or interface. This strong localization allows the near-surface field to dominate the optical interaction, providing a way to probe features smaller than the diffraction limit [3].

Consequently, to directly access the high spatial frequency components necessary for super-resolution imaging, a 'probe' must be positioned within a distance

$$r \ll \lambda, \tag{2.22}$$

ensuring that the evanescent waves remain sufficiently strong to be detected. To give an indication, for most research, $r \lesssim 100\,\text{nm}$ is typically sufficient for visible wavelengths [3].
This near-field condition forms the fundamental operating principle of Scanning Near-field Optical Microscopy (SNOM) and other near-field techniques that enable imaging beyond the classical diffraction limit.

2.5. Grating Couplers

A grating coupler is a periodic structure that consists of alternating etched and unetched regions, placed at the end of a waveguide. Grating couplers are primarily used to couple light from an optical fiber into a waveguide. In this project, they are employed to couple light out of the waveguide.

The key parameters of the grating coupler are defined as follows. The grating period (or pitch) is denoted by Λ. Each period consists of an etched section of length l_e and an unetched section of length l_{ue}. These lengths can differ, and the fraction of each period that is etched is called the *fill factor F* (see Fig. 2.3).

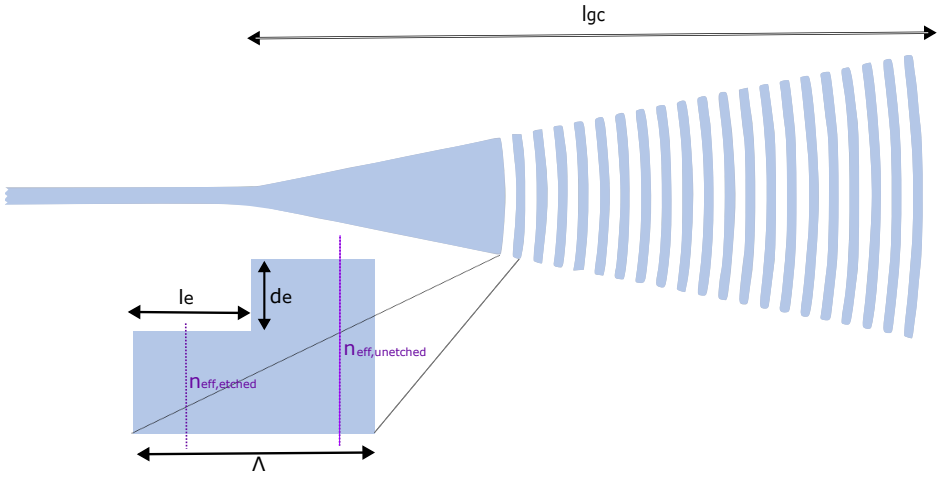

Figure 2.3: Top-view of a gating coupler with a side view of a unit cell showing its parameters.

Other relevant variables of the gating coupler, influencing the behavior of light, are related to the effective refractive index. The regular refractive index n could be written as:

$$n = \frac{c}{v} = \frac{\lambda_0 f}{\lambda f} = \frac{\lambda_0}{\lambda} = \frac{\frac{2\pi}{k_0}}{\frac{2\pi}{k}} = \frac{k}{k_0}, \tag{2.23}$$

where λ_0 and k_0 represent the wavelength and wave-vector in free-space (vacuum) respectively. For grating couplers, it is convenient to use the *effective index* n_{eff}, which characterizes how light propagates in a guided mode along a waveguide. This concept will be used later to derive the grating equation, based on the approach of Zhao and Fan [27].

The effective index accounts for the confinement of the electromagnetic field in the waveguide core and its interaction with the surrounding cladding. It is formally defined as the ratio of the speed of light in vacuum to the phase velocity of the mode along the propagation direction (z-axis):

$$n_{\text{eff}}(\Lambda, pol, m) = \frac{c}{v_z}, \tag{2.24}$$

where v_z is the phase velocity of the mode along z. The value of n_{eff} depends on the mode profile (indexed by m), the polarization of the mode (pol), and the period (Λ) of the grating. All these factors influence how the electromagnetic field is distributed between the core and cladding.

Analogous to Eq. 2.23 for the refractive index, the effective index can be expressed using the propagation constant β of the mode:

$$n_{\text{eff}}(\Lambda, pol, m) = \frac{\beta}{k_0}, \tag{2.25}$$

Since the mode profiles differ between the unetched and the thinner etched parts of the grating coupler, the effective index does as well. To simplify the denotation of the effective index one shall write: $n_e \equiv n_{\text{eff},e}(\Lambda, m)$ and the unetched part as $n_{\text{ue}} \equiv n_{\text{eff,ue}}(\Lambda, m)$.

With the key parameters of a grating coupler defined, one can obtain a restriciton on the period Λ by looking at phases. Grating couplers allow light to transfer between a guided mode in the waveguide and a radiated mode in free space. This transfer is enabled by the grating's periodic structure. One can express the accumulated phase per grating period as the sum of the contributions from the etched and unetched regions:

$$\phi_\Lambda = \frac{2\pi n_e l_e}{\lambda} + \frac{2\pi n_{\text{ue}}(\Lambda - l_e)}{\lambda}, \tag{2.26}$$

where $m \in \mathbb{Z}$ and $k_0 = 2\pi/\lambda$ is the free-space wavenumber. On the other hand, constructive interference requires that the phase of the guided mode matches the phase of the radiated wave over one grating period Λ. This ensures coherent addition of the light emitted from each grating period.

The guided mode propagates along the waveguide with propagation constant β, accumulating a phase of $\beta\Lambda$ per grating period. Concurrently, the radiated wave propagates at an angle θ with respect to the grating normal. In this configuration, the radiated wave travels a distance of $\Lambda \sin\theta$ along the waveguide axis per grating period, accumulating a phase of $k_0 n_{\text{clad}} \Lambda \sin\theta$, where $k_0 n_{\text{clad}}$ is the wavenumber in the cladding.

Under these conditions, the accumulated phase of the guided mode per grating period can be expressed as:

$$\phi_\Lambda = \beta\Lambda = 2\pi m + k_0 n_{\text{clad}} \Lambda \sin\theta, \tag{2.27}$$

where $m \in \mathbb{Z}$ is the diffraction order, $k_0 = 2\pi/\lambda$ is the free-space wavenumber, n_{clad} is the cladding refractive index, and θ is the emission angle.

By matching the phases and comparing Eq. 2.26 with Eq. 2.27, the grating period Λ can be determined as

$$\Lambda = \frac{\lambda + l_e(n_{\text{ue}} - n_e)}{n_{\text{ue}} - n_{\text{clad}} \sin\theta}. \tag{2.28}$$

This expression usefully gives the grating period required to couple light out of the waveguide at angle θ. This means that, for a fixed detector position and emission angle relative to the grating coupler, an initial pitch Λ can be calculated to guide the design process.

By approximating the effective index over one grating period as a weighted average [28], $n_{\text{eff}} = F \cdot n_{\text{ue}} + (1 - F) \cdot n_e$, Eq. 2.28 can also be written as:

$$\Lambda = \frac{\lambda}{n_{\text{eff}} - n_{\text{clad}} \sin\theta}. \tag{2.29}$$

2.6. Fabry-Pérot Interferometry

Microscopy techniques that involve scanning in the near field are highly sensitive to small spatial disturbances. Such perturbations directly influence the resulting interference pattern, especially in configurations where a cavity is formed—leading to a denser and more sensitive interference structure. This section introduces the mathematical treatment of interference effects specific to SNOM setups, where Fabry-Pérot-like behavior becomes relevant due to the cavity geometry. By understanding the math, one would know how to reduce noise and gain insight into calibrating a SNOM system.
The theoretical method adopted here is adapted from the approaches described in [21, 23, 25], which share a similar structure.

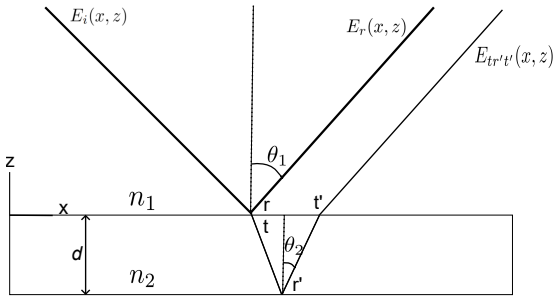

Figure 2.4: The optical path difference leading to a phase shift occuring during reflection by a thin film.

Consider an incident field propagating from one medium towards another at an angle θ_1 with respect to the z-axis. The x-axis is chosen to lie in the plane of incidence. The wavenumber in the medium is given by $k_n = \frac{\omega}{v} = \frac{\omega n}{c} = kn$, where $k = \frac{\omega}{c}$ is the vacuum wavenumber. In this way, the incident plane wave field can be written as:

$$E_i(x,z) = rE_0 e^{i(k_n \cdot r)} = E_0 e^{ikn_1(x\sin\theta_1 - z\cos\theta_1)}, \tag{2.30}$$

where the time-dependent factor $e^{-i\omega t}$ is omitted throughout, as it is common to consider only the spatial dependence of time-harmonic fields. $E_i(x,z)$ represents the scalar field amplitude of the incident wave at point (x,z), with amplitude E_0. θ_1 is the angle of incidence with respect to the z-axis in medium 1, and n_1 is the refractive index of the medium of the incident plane, see Fig. 2.4.
The field reflected at the interface $z = 0$, rather than transmitted into the thin film, is given by:

$$E_r(x,z) = rE_0\, e^{ikn_1(x\sin\theta_1 + z\cos\theta_1)}, \tag{2.31}$$

where r is the reflection coefficient at the boundary between medium 1 and medium 2. Another portion of the wave is transmitted into the thin film (medium 2), undergoing refraction according to Snell's law: $n_1 \sin\theta_1 = n_2 \sin\theta_2$.
The transmitted wave is also scaled by the transmission coefficient t, defined such that the transmitted field amplitude is tE_0. Evaluating the transmitted field at the bottom of the slab, i.e., at $z = -d$, yields:

$$E_t(x, z=-d) = tE_0\, e^{ikn_2(x\sin\theta_2 + d\cos\theta_2)}, \tag{2.32}$$

where n_2 is the refractive index of the thin film and θ_2 is the angle of transmission.
From this bottom point, part of the wave is reflected back upward within the slab. At an arbitrary point (x,z) inside the slab, the resulting upward-propagating field is:

$$E_{tr'}(x,z) = tr'E_0\, e^{ikn_2(x\sin\theta_2 + d\cos\theta_2 + (z+d)\cos\theta_2)}, \tag{2.33}$$

where r' is the reflection coefficient at the bottom interface. The vertical distance covered from $z = -d$ back up to the arbitrary point z is $z - (-d) = z + d$, the additional optical path length is $(z+d)\cos\theta_2$.
Evaluating this reflected field at the top interface ($z = 0$) gives:

$$E_{tr'}(x, z=0) = tr'E_0\, e^{ikn_1(x\sin\theta_2 + 2d\cos\theta_2)}. \tag{2.34}$$

By comparing the two successive outward radiating fields: Eq. 2.31 and Eq. 2.34, the successive radiated field has a phase difference of

$$\delta = 2n_2 kdcos(\theta_2) \tag{2.35}$$

compared to it predecessor.

For constructive interference the phase difference between the rays must be an integer multiple m' of 2π, and for destructive interference, the multiple must differ by a factor of π.

$$\begin{aligned} \Delta\phi &= m' \cdot 2\pi && \text{constructive interference,} \\ \Delta\phi &= \left(m' + \frac{1}{2}\right) \cdot 2\pi && \text{destructive interference.} \end{aligned}$$

It is useful to have obtained the optical path difference between two neighboring lightrays. In reality there are more lightrays that interfere with each other when reflectance takes place inside the thin film. In *SNOM* the thin film is merely a free-space cavity between notably the imaged object and a probe. Therefore, one can substitute $n_2 = 1$. When light enters this cavity, part of it is reflected

back out at each interface, while the remainder continues to propagate within the cavity, undergoing multiple reflections.

The same approach used for single-reflection thin-film interference can be applied for multiple reflections, incorporating the phase-shift term δ from Eq. 2.35. Multiple reflections inside the cavity, denoted by M, contribute an additional factor of $(r^2 e^{i\delta})^M$. The outgoing field consists of two transmitted components: one transmitted directly through the cavity, and one transmitted after undergoing M internal reflections. See Fig. 2.5.

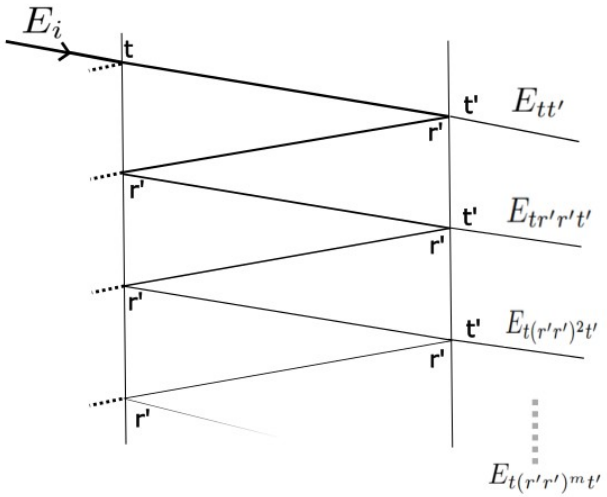

Figure 2.5: In a cavity between two media, lightrays bounce back and forth unless it radiates away through transmission. The final transmission leads to the Fabry-Pérot effect.

By following the light path in this manner, the successive contributions to the transmitted field outside the cavity become, relative to the initial field:

$$\begin{aligned} E_{tt'} &= E_i tt' \qquad (2.36)\\ E_{tr'r't'} &= E_i tr'r'e^{i\delta}t' \\ E_{t(r'r')^2t'} &= E_i t\left(r'^2 e^{i\delta}\right)^2 t' \\ &\vdots \\ E_{t(r'r')^m t'} &= E_i t\left(r'^2 e^{i\delta}\right)^m t' \qquad (2.37) \end{aligned}$$

The total reflected field is obtained by summing over all multiple reflections. This infinite geometric series converges under the condition $r'^2 e^{i\delta} < 1$, yielding

$$\begin{aligned} E_r &= \sum_{m=0}^{\infty} E_i tt' \left(r^2 e^{i\delta}\right)^m \\ &= \frac{E_i tt'}{1 - r'^2 e^{i\delta}} \\ &= \frac{E_i tt'}{1 - Re^{i\delta}} \end{aligned}$$

where the substitution $R = r'^2$ has been introduced. If one further assumes $t \approx t'$, it is convenient to define $T = tt'$. Based on this field expression, the corresponding intensity distribution of the Fabry–Pérot resonance can be calculated as

$$
\begin{aligned}
I_r = |E_r|^2 &= \frac{I_0 T^2}{|1 - Re^{i\delta}|^2} \\
&= \frac{I_0 T^2}{1 + R^2 - 2Rcos(\delta)} \\
&= \frac{I_0 T^2}{(1-R)^2 + 4Rsin^2(\delta/2)} \\
&= \frac{I_0}{1 + \frac{4R}{1-R^2} sin^2 \frac{\delta}{2}} \qquad (2.38) \\
&= \frac{I_0}{1 + F sin^2 \frac{\delta}{2}} \qquad (2.39)
\end{aligned}
$$

Here, $I_0 = |E_0|^2$ is substituted, and the trigonometric identity $\cos\delta = 1 - 2\sin^2\left(\frac{\delta}{2}\right)$ is applied. The coefficient of finesse is introduced as $F \equiv \frac{4R}{(1-R)^2}$.
By comparing Eq. 2.38 with the illumination source, the transmission ratio is obtained as

$$\frac{I_t}{I_i} = \frac{1}{1 + F sin^2 \delta/2}, \qquad (2.40)$$

which indicates the spatial behavior of the Fabry-Pérot effect. This equation is known as the Airy function and is demonstrated in Fig. 2.6.

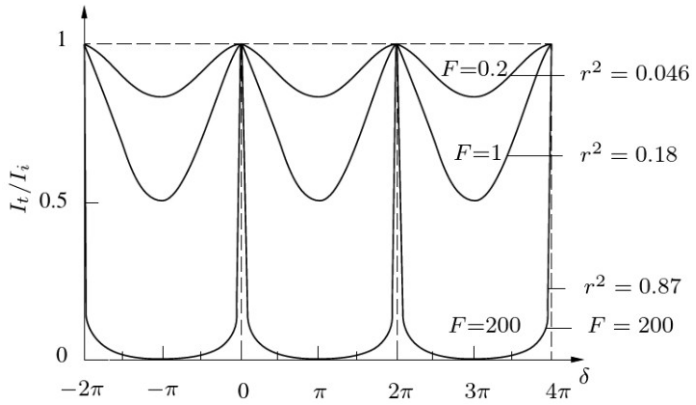

Figure 2.6: The airy function, indicating the intensity behavior as a function of the phase shift for different Finesse coefficients. [25]

In this figure one could observe that higher finesse causes sharper spikes in the distribution. And since $F \sim r^{-2}$ the higher the reflectance is, the narrower the spikes.
During raster scanning, the separation $d(x, y)$ varies slightly, modulating the phase shift $\delta(x, y)$ and introducing high-frequency intensity fluctuations in the 2D image. In the context of raster scanning with a varying cavity length $d(x, y)$, it can be more insightful to rewrite equation 2.40 as:

$$I_{\text{measured}}(x, y) = I_{\text{NF}}(x, y) \cdot \frac{1}{1 + F \sin^2 \delta(x, y)/2}, \qquad (2.41)$$

where $I_{\text{NF}}(x, y)$ is the true Near-Field intensity of the sample and the second term captures the modulation induced by the Fabry-Pérot cavity formed between the waveguide 'tip' and the sample. These fluctuations constitute Fabry-Pérot noise superimposed on the near-field signal, with amplitude and spatial frequency determined by the cavity Finesse F and the tip-sample distance stability.

3

Experimental Method

This chapter describes the integration of optical, mechanical, and fabrication techniques used to implement the PIC-based microscopy system. It emphasizes how light is coupled, guided, and detected within the setup, and how both photonic and imaging samples were designed and fabricated to meet the system constraints.

Section 3.1 details the components of the experimental setup. The design of PIC- and imaging sample is discussed in section 3.2, while motion and control systems—including stages, piezo motors, and scanning patterns—are explained in section 3.3.

3.1. Experimental Setup

The path followed by the signal to produce an image is summarized in Table 3.1. Presenting the setup in this stepwise manner clarifies how the signal evolves through the system. The underlying principles of the experimental approach are explained in detail according to these steps, including justifications for the chosen components and system parameters.

Table 3.1: Overview signal propagation in experimental setup

Step	Description
1.	Generating light in the optical fiber
2.	Coupling light from the source fiber into the waveguide
3.	Through-waveguide propagation towards scanning sample
4.	Reflection on scanning sample
5.	Through-waveguide propagation towards detection system
6.	Collecting light at the detector

Throughout the explanation, the schematics of this setup, shown in Figure 3.1 could serve as a visual reference that can be consulted. Subfigure 3.1a provides a detailed view focused on the PIC region, while subfigure 3.1b presents a more general overview of the full experimental set-up. Together, these schematics support the reader in following the explanation of the optical path step by step.

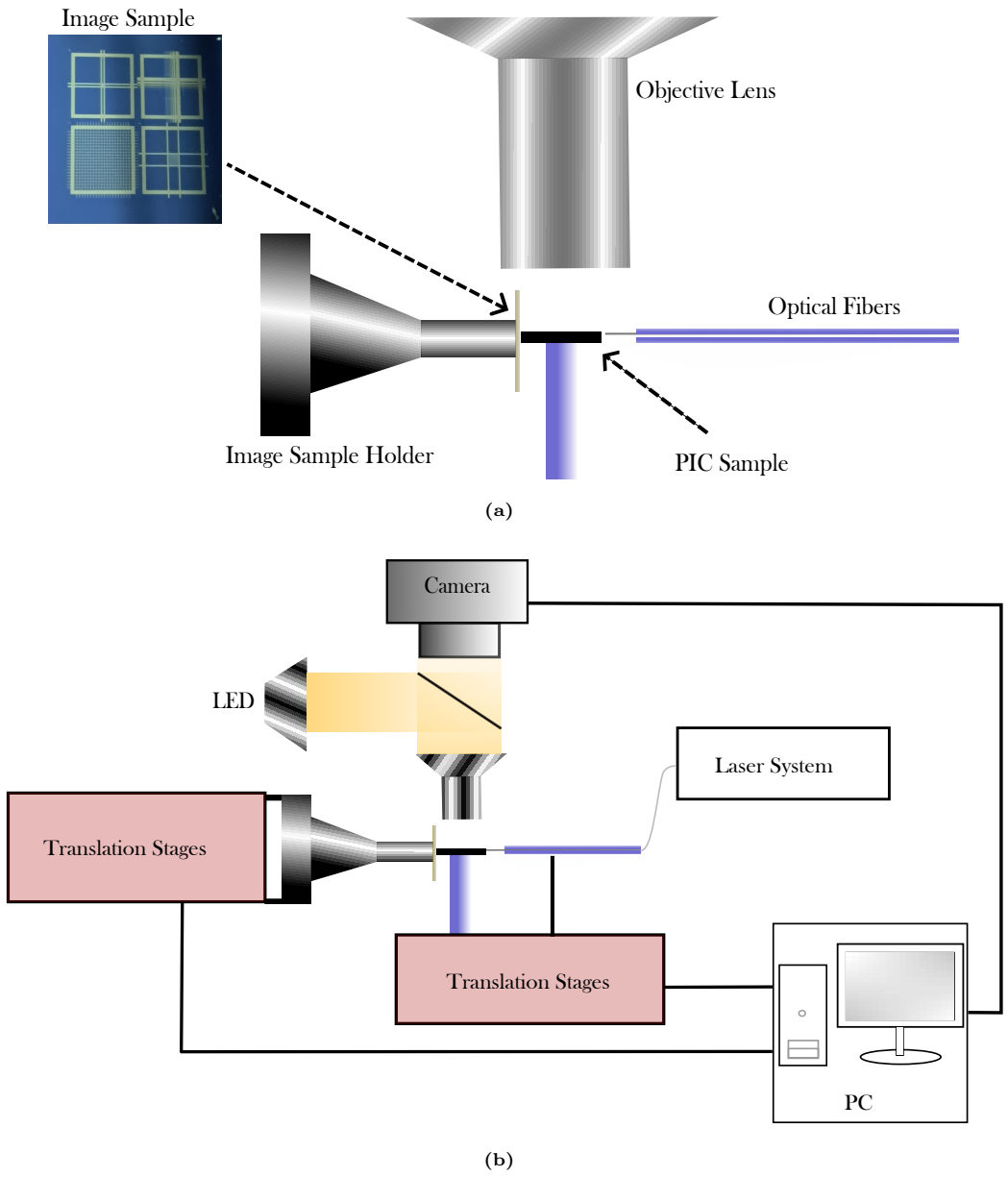

Figure 3.1: Schematics of the waveguide-based imaging setup. (a) Detailed view of the integrated circuit region, showing the optical fibers, the PIC sample with integrated waveguides, the imaging sample containing the target image, and the objective lens, which is used for both light collection and imaging. (b) General schematic of the full setup, consisting of the laser system, camera, illumination stage (lamp), translation stages for precise positioning, and a PC for system control and image acquisition.

1. Generating light in the optical fiber

Light is generated by two different methods.

The first source is a single-mode, polarization-maintaining laser operating at a wavelength of 780nm. This source is particularly useful when higher optical powers are required. Moreover, this wavelength coincides with the optimal transmission window of the optical fibers, where they operate most efficiently.[29] These fibers also preserve polarization and can be directly connected to polarization-sensitive components.

The second source—and the one primarily used in this project—employs a laser diode driven by a current source. A current source supplies electrical power to a laser diode, which emits light at 881, nm. The emitted beam is linearly polarized and coupled into a single-mode fiber. However, the stability

of the laser diode is limited around 10mA. A basic stability test of this configuration is presented in Appendix C.

High optical power is not always desirable, since excessive power makes it difficult to visually distinguish scattered from reflected light in the camera image. To address this, an adjustable attenuator is used: it allows the current source to operate in its stable regime while reducing the effective optical power. The trade-off, however, is the loss of polarization control, since the attenuator is not polarization-maintaining and introduces polarization-dependent loss.

High optical power is not always desirable, as it can make it difficult to distinguish scattered light from reflected light in the camera image. To address this, an adjustable attenuator is used. This allows the laser diode to operate at a stable current, while the output power is reduced after emission. In this way, the output power remains controllable without modifying the laser drive conditions. The trade-off is that the attenuator is not polarization-maintaining. The attenuated light is ultimately coupled into a tapered fiber.

2. Coupling light from the source fiber into the waveguide

To enable waveguide-based microscopy, light must be efficiently injected into the photonic integrated circuit (PIC). This is accomplished by placing an optical fiber in close proximity to the input facet of the waveguide, aligning it such that light can be coupled directly into the waveguide core [7]. This method, commonly referred to as side-coupling (sometimes called edge coupling), typically involves positioning the fiber laterally at the polished edge of the chip . Figure 3.2 illustrates this configuration.

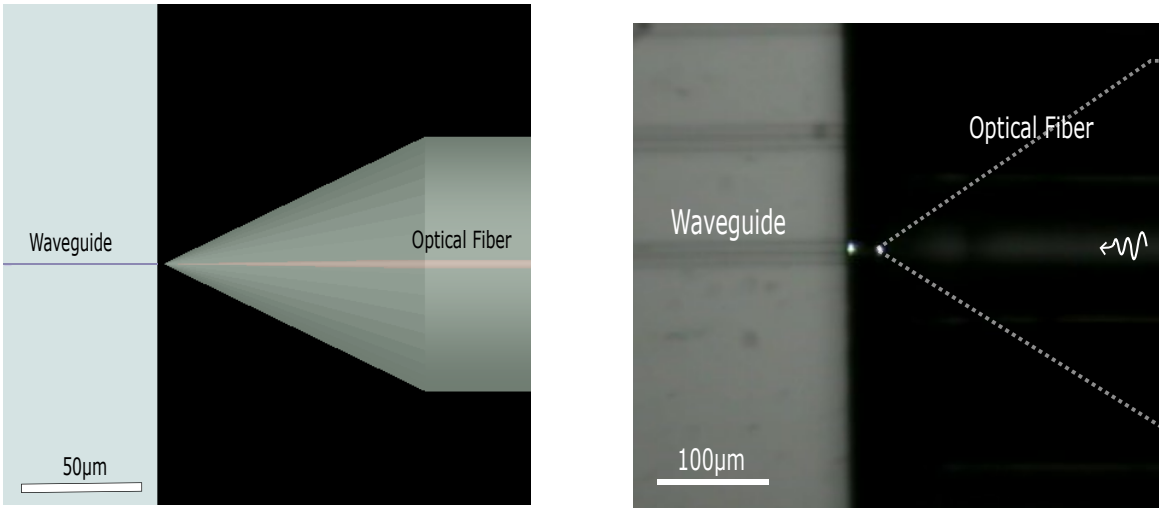

(a) Sketch of side-coupling showing the proportions.

(b) Optical image of side-coupling with an 10x zoom objective.

Figure 3.2: Side-Coupling of a tapered fiber of 125μm diameter into a 500nm wide waveguide a tapered fiber

Side-coupling is chosen in this context due to its relatively straightforward alignment process. Grating coupling for light insertion requires precise fabrication of diffractive structures and may have narrower bandwidth or polarization sensitivity. Furthermore, compared to permanently bonded edge-coupled solutions, this method offers greater flexibility and ease in swapping waveguide samples facilitating scalability in testing different PIC designs.

For the coupling, tapered fibers are used for enabling for focusing light precisely for efficient coupling. The spot size is $(3.5 \pm 0.5\ \mu\text{m})$ at a working distance of $(13 \pm 2\ \mu\text{m})$ [29].

Side-coupling is implemented using a *V-groove array*. This means that each fiber is positioned in a precisely etched V-shaped trench to ensure accurate alignment and stable positioning.The V-grooves are embedded in a beam-shaped piece of silicon, which maintains the fixed spacing and provides mechanical support. The tapered fiber tips protrude approximately $4.5 \pm 0.5\,\text{mm}$ from the front edge of the chip, with a maximum protrusion difference of $15\,\mu\text{m}$ among the fibers. Furthermore, the V-groove array

holding four polarization-maintaining (PM) tapered optical fibers with a core/cladding diameter of $5/125\,\mu$m and a center-to-center spacing of $250\,\mu$m.
While this approach allows for precise passive alignment, the relatively large protrusion becomes a limiting factor for scalability. Given that the working distance of the tapered fibers is only $13 \pm 2\,\mu$m, such variation can lead to significant focus mismatch across channels, reducing coupling efficiency and making reproducible alignment across multiple samples more challenging.

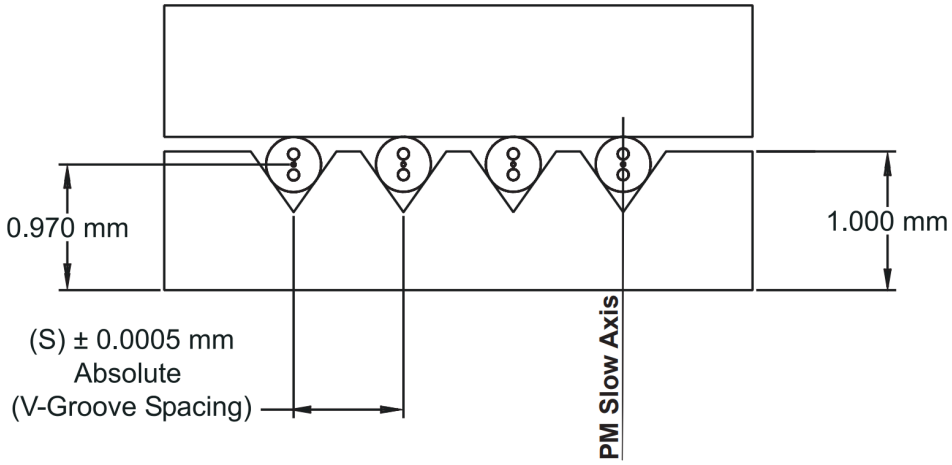

Figure 3.3: Cross section of the V-groove assembly used from OZ optics. [29]

This single silicon element can be easily integrated into a custom mounting structure—such as a 3D-printed *fiber holder*—that secures the array during alignment with the photonic chip.

When it comes to the *side-coupling positioning* procedure, it should be noted that there is a scale difference between the tapered fiber and the waveguide, which highlights the level of precision required for successful coupling (see Fig. 3.2a). The fiber-to-waveguide coupling was monitored in real time using a camera mounted above the PIC system, as shown in Fig. 3.7b.
A coarse manual alignment is performed using a screw-based positioning mechanism. In this system, a metal adjustment screw pushes one side of a plastic (polymer) *translation stage*, while a spring on the opposite side provides restoring force and mechanical contact.
Fine positioning is achieved using *piezoelectric actuators*, digitally controlled via dedicated software. These actuators provided a positioning precision of approximately 30 nm [30], which is sufficient to align the beam with a waveguide measuring 500×250 nm.

Coupling had to be repeated each time the sample was changed. Because misalignment may occur gradually over time, the alignment must be periodically checked. The detailed alignment procedure is provided in Appendix A. It is worth noting that a more permanent coupling would likely improve stability, but would reduce the flexibility to interchange PIC samples.

3. Through-waveguide propagation towards scanning sample

When coupled into the PIC, light must propagate from the fiber-side of the chip towards the imaging sample, see Fig. 3.4.

The exact waveguide design varies and will be discussed in Section 3.2.

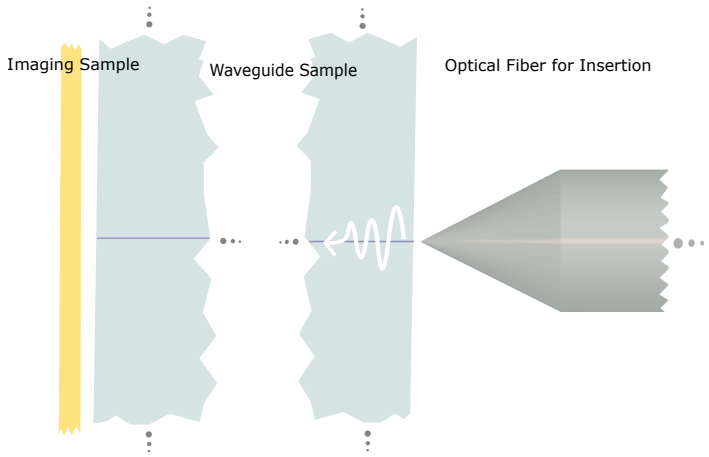

Figure 3.4: On-chip propagation towards the imaging sample

4. Reflection on scanning sample

When light exit the terminating waveguide, it diverges, as shown in Fig. 3.5. After an abrupt termination, the light spreads approximately linearly. [7, 31]

Figure (a) shows the waveguide sample (right) parallel to the scanning sample (left); if they were not aligned, the samples would collide during scanning. Figure (b) shows a simulation of the electric field emerging from the waveguide and propagating through air toward the imaging sample.

The emitted light propagates towards the target object. Upon reflection, the image information—encoded in the intensity distribution of the reflected light—returns towards the same waveguide. Since the light beam diverges upon leaving the waveguide, the amount of reflected light depends on both the divergence and the reflectivity r of the surrounding materials.

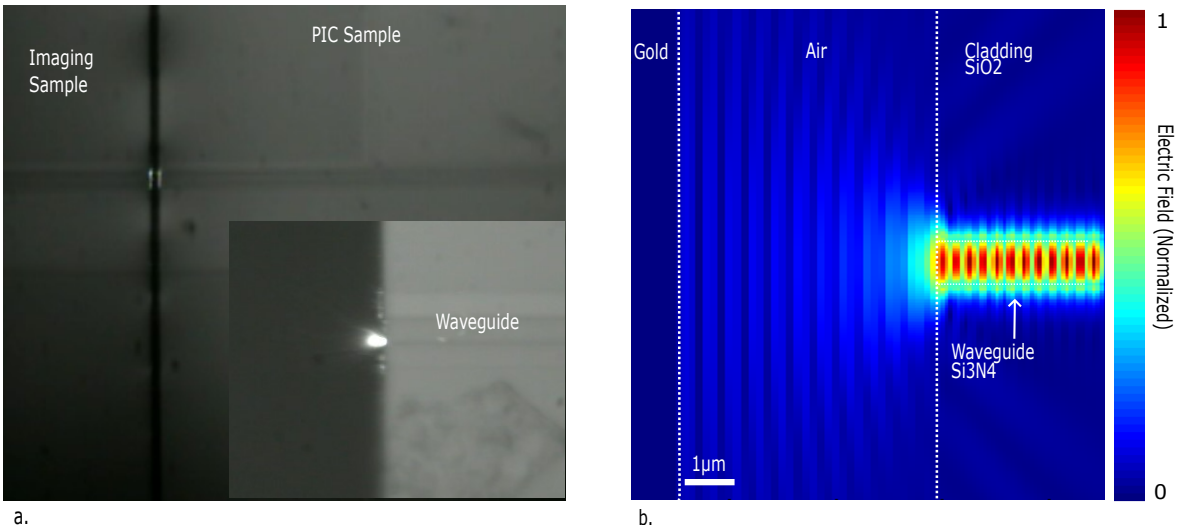

Figure 3.5: (a) Top-view optical image of light exiting the waveguide sample and interacting with the scanning sample. (b) Simulated electric field distribution for the same configuration, where light exits the Si_3N_4 waveguide and propagates towards a gold surface.

5. Through-waveguide propagation towards the detection system

After interacting with the sample, the light propagates back through the same waveguide, now carrying the image information. At the PIC, the returning signal is directed into the same input waveguide and

then diverted via a branching structure towards the detection path. In this way, the portion of light intended for detection is separated from the rest of the circuit. The design of these PIC structures, including the branching and coupling elements, is described in more detail in Section 3.2.

6. Collecting light at the detector

A photodetector is used to collect light and thus convert photon flux into an electrical signal suitable for analysis. In this project, a Avalanche PhotoDiode (APD) photodetector is used. Such detectors offer high sensitivity and time resolution, making them ideal for low-light applications. [32]

The APD used in this study was the SPCM-AQRH module from Excelitas. It operates over a spectral range of 400–1064 nm and provides a photon detection efficiency (PDE) of approximately 45% at 830 nm [33]. This is close to the operational wavelength of 881 nm used in this work, for which the PDE is expected to be slightly lower, but still within acceptable limits. Another relevant characteristic of the SPCM-AQRH-12-FC module is its low dark count rate, specified by the manufacturer to be below 500 cps. The dark count rate can be readily measured before experiments to account for device-specific variations.

The electrical pulses generated by the detector were processed by time-correlator hardware, which associates each photon event with a time reference. In this work, two different correlators were employed to measure photon count rates and transfer the data to a PC via USB: a TimeTagger from Swabian Instruments, and the electronics module supplied with the SNSPD driver from Single Quantum, here connected to the APD. By converting the detection events into counts per second, the system provides a quantitative measure of light intensity, from which image contrast can be extracted to form a digital image.

3.2. Sample Design

In this section, the sample designs are presented. Section 3.2.1 addresses the choice of waveguides for all PIC samples. The two distinct PIC architectures, a *fully side-coupled* system and a *grating-coupler-based* system, are described in Sections 3.2.2 and 3.2.3, respectively. Finally, the design of an image sample is outlined in Section 3.2.4.

3.2.1. Design of Waveguides in the PIC Sample

The buried channel waveguide geometry provides mechanical protection and optical confinement. A larger waveguide cross section can, in practice, make side coupling more tolerant to alignment errors, since the tapered fiber tip has more margin. So a wider waveguide is generally preferred to ease alignment and increase coupling efficiency.

However, the dimensions must still be chosen carefully to ensure good mode matching. In addition, the waveguide dimensions must be designed to support single-mode operation. This single-mode operation is desired for two main reasons:

Firstly, the Gaussian-like shape of the fundamental mode is ideal for precision microscopy, as it enables well-defined and stable light profiles.

Secondly, multimode propagation tends to behave inconsistently in bent waveguides, such as those used in this work, since higher-order modes may not maintain their spatial profile after bending, leading to mode distortion and increased loss.

To balance these size requirements, the waveguide width was optimized by performing modal analysis using finite-difference eigenmode (FDE) simulation software.

The waveguide height was set to the maximum possible height possible in production, which is$h = 250\,\text{nm}$. To determine the maximum width w that ensures single-mode operation, a parameter sweep was performed with a resolution of 50 nm. At each step, the supported modes were analyzed, and the largest width was selected such that no higher-order modes with effective index n_{eff} exceeding that of the cladding were present. Because if the effective index of a certain mode would exceed that of the cladding, the mode would leak into the cladding.

Supporting modes with $n_{\text{eff}} > n_{\text{cladding}}$ hon the other hand, would indicate guided multimode

operation, which is undesirable for this experiment. By this approach, the optimal waveguide cross section was determined to be $w \times h = 500\,\text{nm} \times 250\,\text{nm}$, which supports single-mode operation. An illustration of mode comparison is shown in Fig. 3.6.

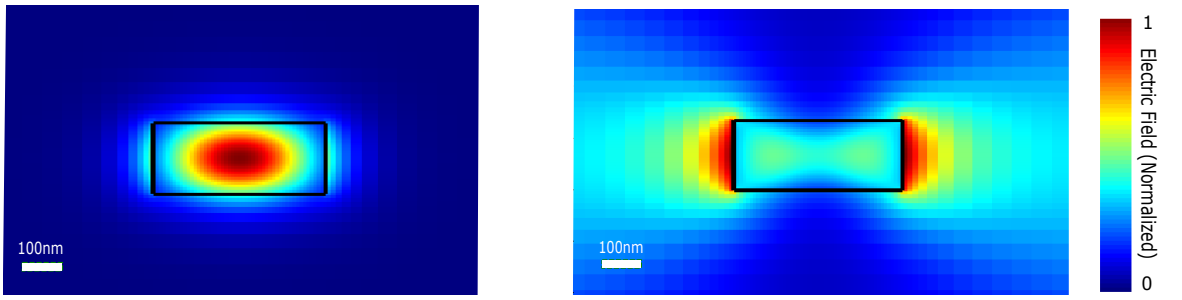

(a) **(b)**

Figure 3.6: Mode profiles in a 500 nm × 250 nm waveguide. (a) the fundamental mode and (b) a higher-order mode, which has $n_{\text{eff}} < n_{\text{clad}}$ ($1.43 < 1.45$), indicating it is not guided.

The fabrication process was not part of this project, but is summarized here for completeness. First, SiN is deposited on a silicon substrate with a silicon dioxide (SiO_2) layer. A resist layer is then patterned by electron-beam lithography. After exposure and development, the pattern is transferred into the SiN layer by etching. Finally, a SiO_2 cladding layer is deposited to complete the structure.

Since minimizing the gap between the waveguide and the scanning sample is critical, the end facet of the waveguide chip must be as straight and smooth as possible. This ensures precise alignment between the waveguide sample and the flat surface of the scanning sample, as illustrated in Fig. 3.5. To achieve this, the waveguide chip is cleaved along predefined guide lines during fabrication, aiming to produce a clean edge perpendicular to the surface, though not necessarily along the depth of the waveguide.

3.2.2. Fully Side-Coupled PIC Design

The initial waveguide sample was one that is based on a side-coupling for both light insertion, as for the collection, after light is reflected on the image sample.This PIC sample design consists of two branches.

The first segment serves as the input source waveguide, which follows a quarter-circle bend with a radius of $r = 100\,\mu\text{m}$. This is followed by a straight section of $50\,\mu\text{m}$, after which another quarter-circle bend connects it to a long, straight output waveguide. From there, the light is directed toward the scanning sample. The chosen dimensions match the $250\,\mu\text{m}$ V-groove separation, and the use of relatively large bend radii helps to minimize bending-induced (excess) losses [34].
The second branch is a straight path from the imaging sample towards the fiber for light collection. Upon reflection this light contains the image data in the form of intensity.

The total μ-shape of the waveguides can be seen in Fig. 3.7a. A photograph of the coupling is shown in fig. 3.7b.

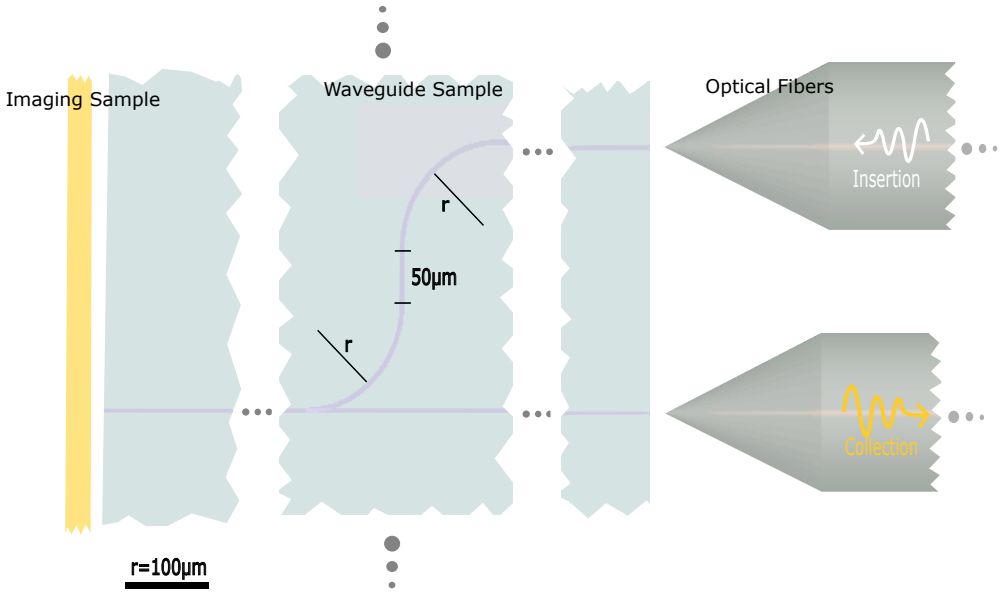

(a) General overview of the PIC-system with the Fully Side-Coupled Waveguide. This waveguide sample (middle) is placed between the scanning sample (left) and the optical tapered fibers (right). The width of the waveguide is increased by a factor of 10 for visual clarity.

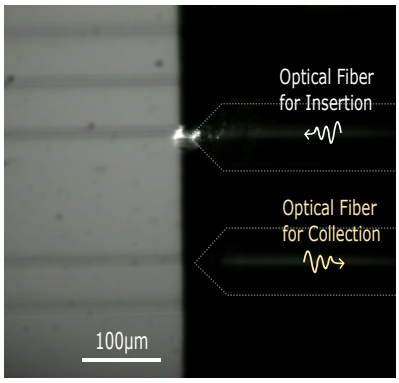

(b) Optical image of the side coupling between the optical fibers and the waveguide

Figure 3.7: The design of the waveguide sample for fully side-coupled imaging requires one optical fiber for light insertion and one for collection.

Ten μ-shaped waveguide structures were fabricated on a single chip to account for quality variations. Also, the side-coupling regions are prone to get damaged. A more complete design could be found in Appendix B.

3.2.3. Grating-Coupler-Integrated PIC Design

Although the waveguide sample described in the previous section offers a straightforward configuration, several challenges emerge when employing side coupling for both the injection and collection branches. The main issues are:

1. Scattered light from the injection fiber is detected directly by the collection fiber, without going through the PIC system, causing background noise.
2. Two tapered fibers—one for light injection and one for collection—must be precisely aligned in all spatial degrees of freedom. This combination of side coupling is prone to systematic errors.
3. When aiming to scale the design for parallel scanning of multiple waveguides, many fibers and detectors are needed. Furthermore, the overall design becomes increasingly asymmetric.

To address these limitations, an alternative waveguide design is proposed. Permanently bonding

optical fibers to the waveguide can improve mechanical stability, but this approach is costly and prevents fiber reuse. Instead, light is coupled into the waveguide without permanent fixation, as illustrated in Fig. 3.8a. The waveguide then branches into four separate paths, resulting in four exit points at the image side (Fig. 3.8b).

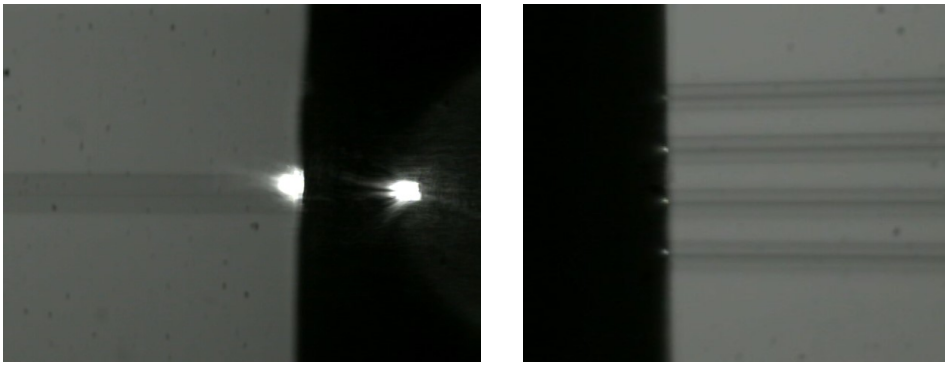

(a) Single side-coupling. **(b)** Four-branches at the image side.

Figure 3.8: (a) Side-coupling is (only) needed to insert light in one-branch, (b) the single waveguide splits up in four and at the image side there are four branches exiting enabling multi probe scanning.

Upon reflection, instead of leading the light towards another optical fiber, it is split up towards a grating coupler. These couplers allow for vertical coupling of light. Because of required symmetry of the branches, similar Bézier curves, chosen for its smooth transitions, lead each branch to its own grating coupler, which paramaters are chosen to fit in between waveguide branches and the field of view of the camera.

An analysis of the grating coupler parameters can be found in section 4.1.5. The format of the The angle and radius of the grating coupler are constrained by both the physical layout of the waveguides and the imaging system. If the couplers are too large, they may overlap with neighboring waveguides, while if they are too small, the grating will not cover enough camera pixels to be clearly imaged.

To ensure that the grating coupler is well captured by the camera, its size must cover multiple pixels on the sensor. The Watec WAT-120N+ camera has a sensor of 752×582 pixels (horizontal $\times$ vertical) spanning a field of view (FOV) of 245.5 μm $\times$ 190.0 μm. Dividing the FOV by the corresponding pixel counts gives an effective pixel size of approximately 325 nm in both horizontal and vertical directions.

A grating coupler is chosen to have a radius of $R = 17$ μm and an opening angle of $\theta = 36°$, which corresponds to a surface area of the circular sector

$$A_{\mathrm{GC}} = \frac{\theta}{360°}\,\pi R^2. \tag{3.1}$$

This area ($\approx$ 283 μm^2) is much larger than the pixel resolution area of the camera $(0.325\ \mu\mathrm{m})^2 \approx 0.106\ \mu\mathrm{m}^2$, while remaining well within the camera's field of view area. The condition is therefore satisfied:

$$A_{\mathrm{pixel}} << A_{\mathrm{GC}} << A_{\mathrm{FOV}}. \tag{3.2}$$

The design is shown in Fig. 3.9, where *Bézier curves* are employed to ensure smooth bending transitions and to minimize radiation loss, which is particularly critical in compact waveguide bends [35].

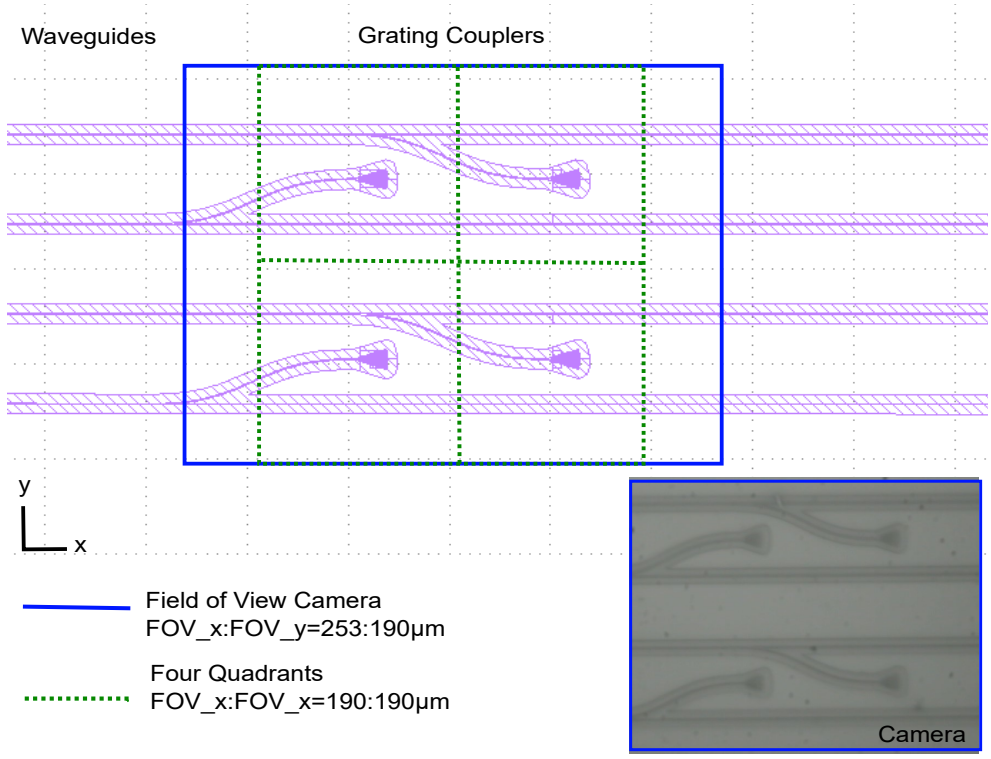

Figure 3.9: The grating couplers are placed such that each of them ends up in its own quadrant and the structure falls nicely in the total FOV.

For an overview of this design, the reader is invited to Appendix B. The grating-coupler-based approach mitigates the aforementioned challenges, because:

1. The grating-coupler it not placed directly next to the input fiber, thereby reducing background noise from scattered light.
2. The number of side couplings is reduced: only a single fiber must be aligned with the waveguide end facet, improving stability and simplifying the alignment process.
3. A single camera replaces many optical fibers and detectors. The compact and symmetric waveguide layout facilitates the integration of additional waveguide structures, enabling faster scanning.

3.2.4. Image Sample Design

To evaluate the microscopy method, a dedicated imaging sample was designed according to the following requirements:

- Lines with varying thicknesses were included to assess the minimum resolvable line width.
- Repetitive structures, such as the text *TUDelft* and coordinate numbers, were placed nearby to serve as positional references during scanning.
- Straight guide lines were added to indicate the scanning region on the camera and to lead the eye toward smaller test structures.

This resulted in the samples shown in Fig. 3.10; further details within the design can be found in Appendix B.

Two material combinations are used (see Fig. 3.10), both produced using a lift-off process.

Firstly, the pattern was fabricated using highly reflective gold contrasted with poorly reflective, highly absorbing silicon, see Fig. 3.10a. In this configuration, optical contrast arises because incoming light is either reflected by the gold or absorbed by the silicon.

Secondly, the pattern was fabricated with a gold layer on Lithium Niobate ($LiNbO_3$, abbreviated as LN) instead of absorbing silicon. Although the material appears yellow in Fig. 3.10b, at a wavelength of 881 nm, light is primarily transmitted rather than absorbed. Here, contrast is generated because light is either reflected by the gold or transmitted through the LN layer.

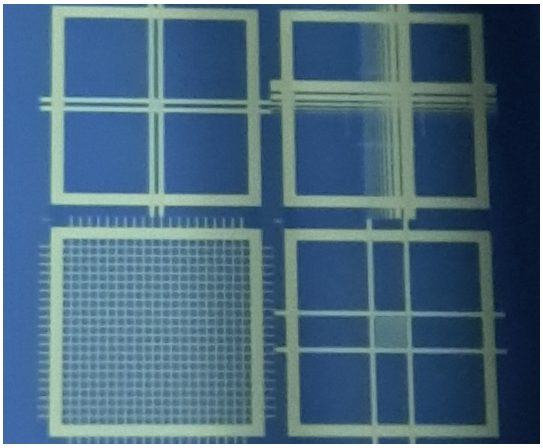

(a) Optical image of a sample in which reflective gold contrasts with the non-reflective silicon substrate.

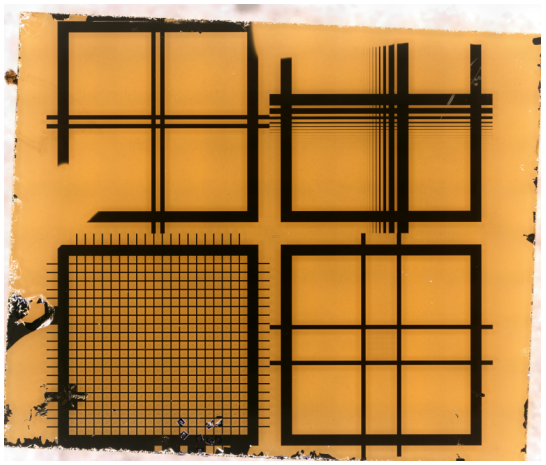

(b) Scanning Electron Microscope (SEM) image of a sample with reflective gold patterns on semi-transparent silicon carbide on a lithium niobate substrate.

Figure 3.10: Image samples produced for this project.

3.3. Motion Control Systems

While previous sections covered the optical signal path, precise motion control is essential for scanning and image stability. Section 3.3.1 covers the mechanical stages, and Section 3.3.2 describes the scanning process.

3.3.1. Mechanical Stages

The imaging setup includes several components mounted on the optical table as independent stages: the *optical fiber stage*, the *waveguide sample stage*, and the *imaging sample stage*. Each stage is described in detail below.

Optical Fiber Stage

The support structure for the V-groove fiber assembly consists of screw-spring-based manual translation stages (Newport/New Focus), which constrain the piezoelectric actuators in position. These metal stages are interconnected and mounted onto the optical table using custom-designed 3D-printed connectors. The full stage is shown in Fig. 3.11.

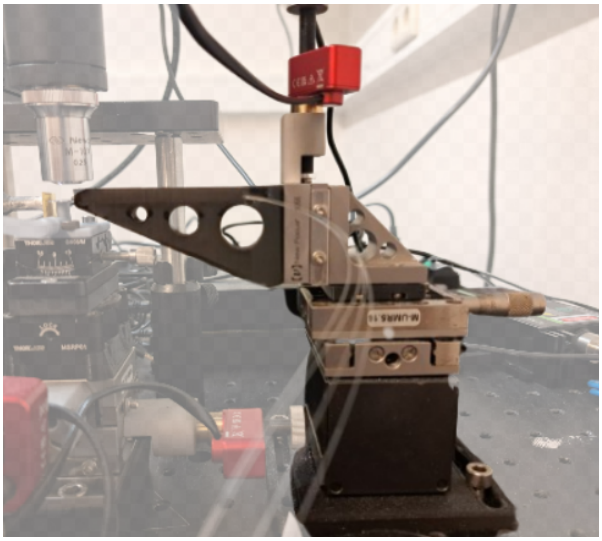

Figure 3.11: Optical fiber stage. The grey screw on the right provides manual translation, while the red piezomotor on top enables precision movement. At the bottom front, four optical fibers are visible; they extend toward the left, where they are secured in a custom-made fiber holder (black).

The fiber assembly (which side-couples into the PIC-sample) is mounted in a custom-designed fiber holder. Two versions of the fiber holder are shown in Figure 3.12. The optical fibers are guided through a groove and secured at the end using a screw that passes through a designated hole. A mounting plate at the back allows the holder to be firmly attached to a translation stage, ensuring stability and precise positioning during alignment.

Figure 3.12a shows the initial fiber holder design, which was used for the majority of this project. A visible issue with this design was a gradual misalignment of the optical fiber along the waveguide width, even when the piezo motors were idle. Given that the waveguides used are only a few hundred nanometers wide, the holder must maintain a high degree of mechanical stability to ensure precise fiber-to-waveguide alignment. Any structural instability in the holder can lead to degraded side-coupling efficiency and negatively impact the imaging results.

For optimal stability, the fiber tip should ideally be positioned at the center of mass of the stage. In the original design, the fiber tip was located 11 cm from the center of the piezo stage. This extended overhang introduces a tilting moment, where small angular deviations can translate into significant lateral displacements—effectively amplifying mechanical errors, leading to noisy images.

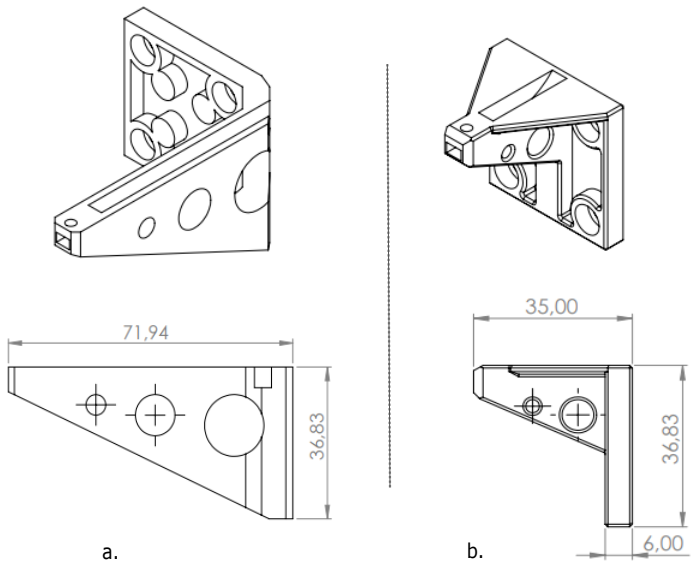

Figure 3.12: 3D-printed fiber holders used to mount the fiber assembly to mechanical stages. Most results were obtained using design (a), which was later replaced by version (b) to improve mechanical stability.

In addition, all actuation forces generated by the motors should ideally act through the system's center of mass to minimize dynamic disturbances. This condition is not met in the initial design due to the asymmetric, protruding arm structure. As noted by Herman Soemers in his book *Design Principles for Precision Mechanics*:

> *"Structures of this kind must be designed as if they were isolated in space. For example, they should be symmetrical about the axis."* [36, Section 1.6.1]

In this experiment, the center of mass is shifted away from the intersection point of the actuator axes, further contributing to instability during operation.

To address these issues, the fiber holder was redesigned, as shown in Figure 3.12b. A comparative analysis of the mechanical stiffness between the two designs is presented in Section 4.1.1. The new design incorporates wing-like supports that connect both the extended arm and the base, improving resistance to lateral disturbances. The fiber protrusion was designed to be reduced by 37 mm—just enough to remain compatible with the overall system layout—while repositioning the fiber tip along the actuator axis to align with the stage's center of mass.

PIC Sample Supporting Stage

The PIC sample is held in place on a dedicated support stage. Similar to the fiber assembly, the structural components are interconnected using 3D printed connectors. The stage includes Newport translation stages that are actuated by two piezo motors, enabling precise movement of the waveguide in the lateral plane (i.e., the plane parallel to the optical table). In addition, a rotating gear mechanism allows for controlled angular adjustment of the waveguide.

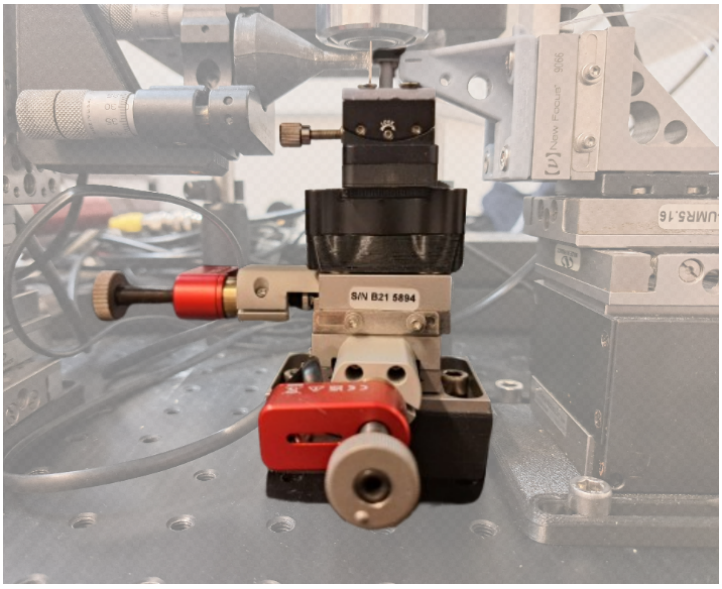

Figure 3.13: PIC (waveguide) stage. The sample is mounted at the top. Two red piezomotors, located at the left and bottom front, provide lateral positioning. A screw on the top left allows for tilt adjustment.

To secure the sample during alignment and operation, a QS-2008 SMD Vacuum Bonder with an electric vacuum wand is used. This system holds the waveguide-containing sample in place through suction, providing stable and repeatable positioning.

Imaging Sample Stage

The imaging sample stage serves to securely hold the sample while enabling precise raster scanning, as shown in Fig. 3.14. The sample is attached to a conical-shaped holder using silver paste, which is then firmly fixed in place by a screw-clamp mechanism that permits two-dimensional rotational adjustment. After measurements, the sample can be detached and the silver paste removed, allowing the holder to be reused.

In this configuration, the sample is mounted on the piezo stage, ensuring mechanical stability during measurements and enabling the SNOM to perform raster scanning. The PIC sample remains fixed, while the imaging sample is translated during the scan. Within the raster scanning process, the lateral motion along the fast axis (left-to-right and right-to-left) is regulated by a closed-loop piezo motor to ensure positional accuracy and repeatability, whereas motion along the remaining axes is controlled with open-loop motors. More about the scanning process is written in the following section (i.e. section 3.3.2).

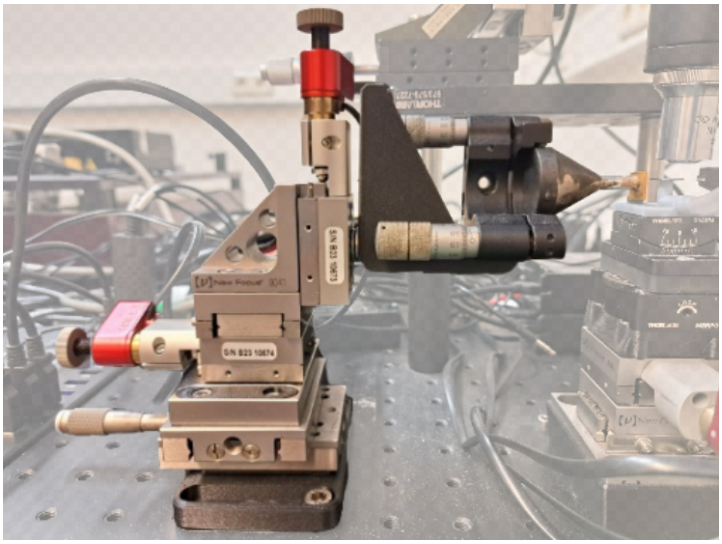

Figure 3.14: Imaging sample stage. The sample is mounted on the black conical holder at the right. Two grey screws in the center provide 2D tilt adjustment to the image sample. Two red open-loop piezomotors (top and left) are visible, while a closed-loop piezomotor is located behind the translation stage. A screw at the bottom left positions the imaging sample close to the PIC sample.

Furthermore, although the stiffness of the setup could be significantly improved, its impact on image quality is smaller than that of disruptions in the side-coupling process. The former introduces minor perturbations, whereas the latter disconnects the entire signal path.

3.3.2. Scanning Process

In this section, the operation of the scanning mechanism is described. In earlier implementations of this setup, three piezoelectric motors—one for each spatial dimension—were coupled to a flexure stage, with a spring providing the restoring force to maintain tension.

Image acquisition in this work is carried out using a step-and-count raster scanning method. In this approach, the sample is incrementally displaced by one of the piezo motors over a defined step size, for example along the x-axis parallel to the optical table. The photodetector converts the incident light into an analog electrical signal, specifically a photocurrent. This signal is then digitized and counted, with the resulting photon counts serving as a measure of the optical intensity. Both the motors and the photodetector are controlled via a set of object-oriented program classes implemented in MATLAB.

In the *stepwise scanning method*, the motor translates the imaging sample by a single step, after which the photodetector records the photon counts over a short integration time, representing the light intensity I. This procedure is repeated N_x times along the x-direction, after which the motor advances one step (i.e., one pixel) in the y-direction to initiate scanning of the next row. In this way, a raster scan is formed. The number of sampling points and the step size are controlled via a MATLAB GUI. A section of the code that illustrates this stepwise process is found in Appendix D.1.

A *continuous* scanning method is employed to reduce image acquisition time. While the raster scan trajectory is preserved, the motor control is modified. Instead of moving in discrete steps, the motor traverses the *entire x-direction* (left to right) in a single motion. During this continuous movement, photon counts are recorded along the full x-direction. This is achieved by matching the scan duration to the photon counting integration time. After the motion is completed, the count values are mapped to their corresponding pixel positions. The motor velocity can be adjusted within the MATLAB GUI. A section of the code that illustrates the principle of the continuous scanning approach in contrast to the discrete method, is found in Appendix D.2.

For the *Grating Coupler* approach, a camera is used in place of the photodetector, and the piezomotor motion is performed manually rather than automatically. Using the standard control software, the motors are moved by a predefined step length, and an image of the illuminated grating couplers is captured at each position. This process is repeated iteratively to cover the desired scanning area.

The captured images are then processed and analyzed in MATLAB. For each image, the region corresponding to the grating couplers is selected, see Fig. 3.15. The average pixel intensity within this region is calculated to measure the light output. In this way, each grating coupler—representing a branch—contributes to quickly form image data of the scanned area.

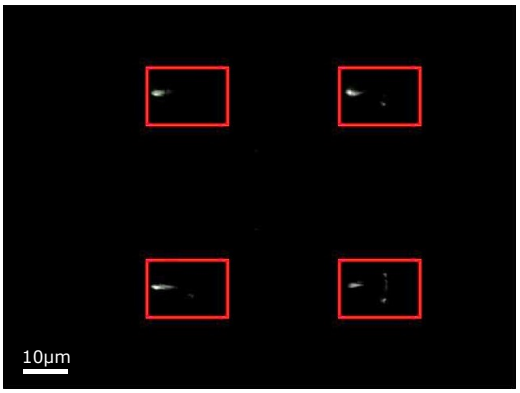

Figure 3.15: A picture of the grating couplers used to analyze the intensity values. To obtain image information, one averages over the intensity values of the pixels within the –via Maltab selected– rectangles surrounding the grating couplers

Using MATLAB's roipoly function, the regions of the grating couplers can be selected more precisely than with rectangular boxes. However, since the pixel intensities outside the grating couplers are observed to be zero, including some of this background in the selection does not affect the relative contrast in the calculated intensities.

4

Results and Evaluation

In section 4.1, both experimental as numerical results about optical performance is shown. Section 4.2 contains imaging results.

4.1. Optical Performance Results

To minimize potential losses in and around the waveguide sample, several factors must be carefully considered. Key sources of disturbance and power loss include:

1. Side-coupling
2. Back-coupling of reflected light
3. Waveguide splitting
4. Dark and background noise
5. Grating parameters

The effect of these factors are discussed in detail in the following sections (4.1.1-4.1.5).

4.1.1. Side-Coupling

As discussed in Section 3.3.1, two fiber holders were employed in the setup. With the initial design (Fiber Holder 1), the side-coupling gradually drifted over time, eventually leading to a complete loss of signal. Because the waveguide is only 500 nm wide, even a slight misalignment between the optical fiber and the waveguide introduces significantly less signal.

This issue motivated the development of an improved design, Fiber Holder 2. To verify that realignment could recover the signal, the effect of lateral displacements on the order of half the waveguide width was investigated.

Figure 4.1a shows the recorded intensity using the previous fiber holder, Fiber Holder 1. A gradual misalignment occurs over time, which can be partially corrected by re-aligning the fiber along the waveguide width (yellow markers). By contrast, Figure 4.1b demonstrates the improved performance of Fiber Holder 2, which provides a more stable signal. In this case, misalignment (yellow, left) occurs only under intentional displacement, and restoring the fiber position (yellow, right) reliably recovers the signal.

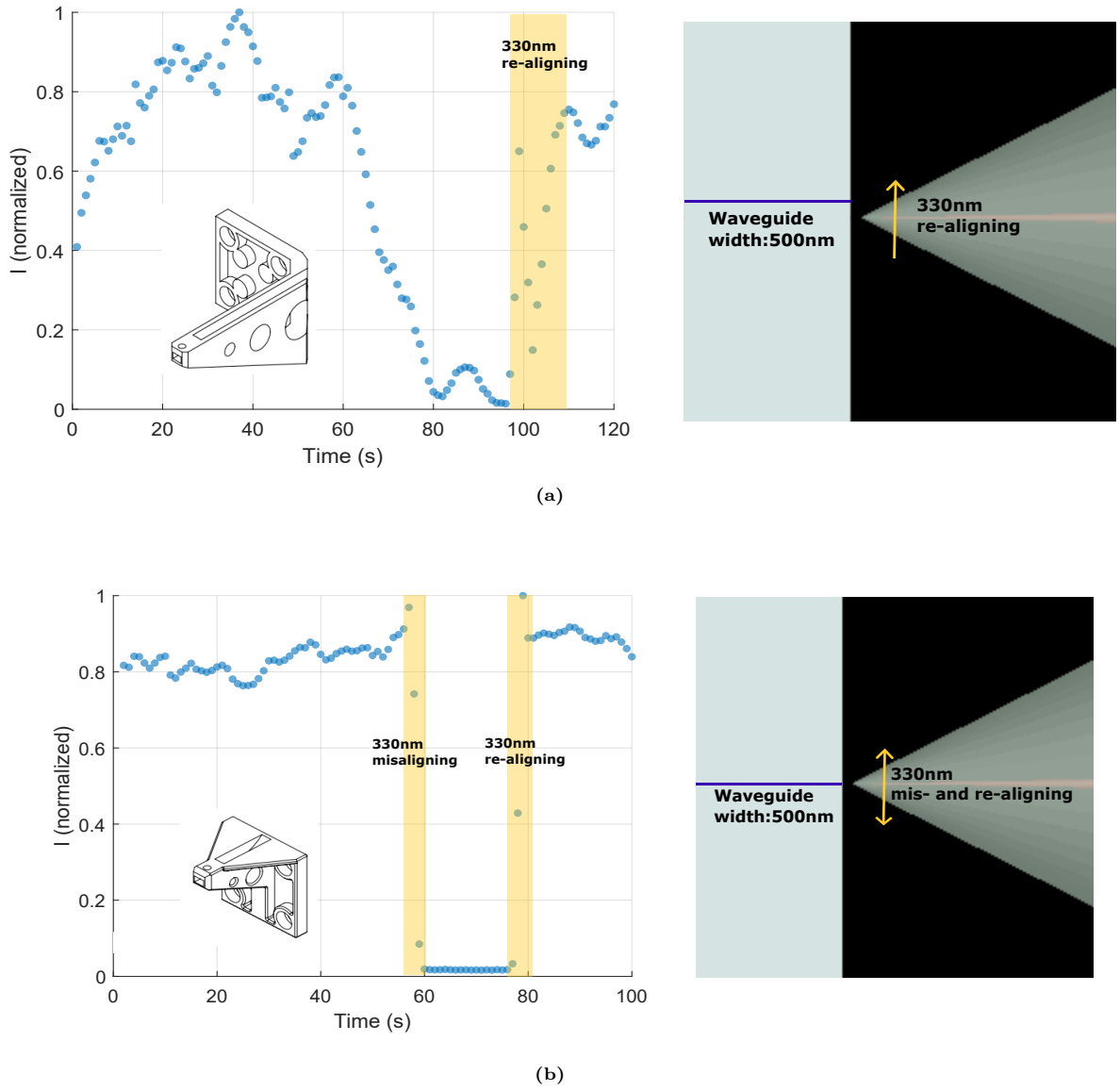

Figure 4.1: Stability analysis of side coupling for (a) Fiber Holder 1 and (b) Fiber Holder 2. The yellow highlights indicate intentional misalignment and re-alignment, illustrating the stability of each setup.

4.1.2. Back-coupling of Reflected Light

When the waveguide and the scanning sample are not perfectly parallel, the separation between them varies across the sample. In addition, imperfections introduced during the cleaving process can cause the waveguide edges to deviate from being strictly perpendicular to the guiding axis. Moreover, the waveguide itself may not be exactly perpendicular to the chip surface, resulting in tilted light emission even when the waveguide and imaging sample are nominally aligned.

To evaluate the impact of these misalignments, the dependence of the setup efficiency on the distance between the waveguide and the imaging sample is examined. Finite-Difference Time-Domain (FDTD) simulations using ANSYS Lumerical are employed to monitor the light transmitted back into the waveguide, which serves as a measure of the coupling efficiency. The transmission can be expressed as:

$$T = \frac{\int_{\text{monitor}} \text{Re}(\vec{P}) \cdot d\vec{A}}{2P_{\text{source}}}, \tag{4.1}$$

where $\vec{P}$ is the Poynting vector, $d\vec{A}$ is the differential surface element oriented along the surface normal, and P_{source} is the source power.

The dependence of transmission on the size of the air gap between the waveguide and the gold-coated scanning sample is presented in Fig. 4.2. This figure shows that the back-coupling decreases exponentially with increasing gap size. An oscillatory behavior with a period of approximately 3 μm indicates the spatial range over which a constant gap must be maintained to avoid interference effects. As expected from Section 2.6, the precise values depend on both tilt and material properties.

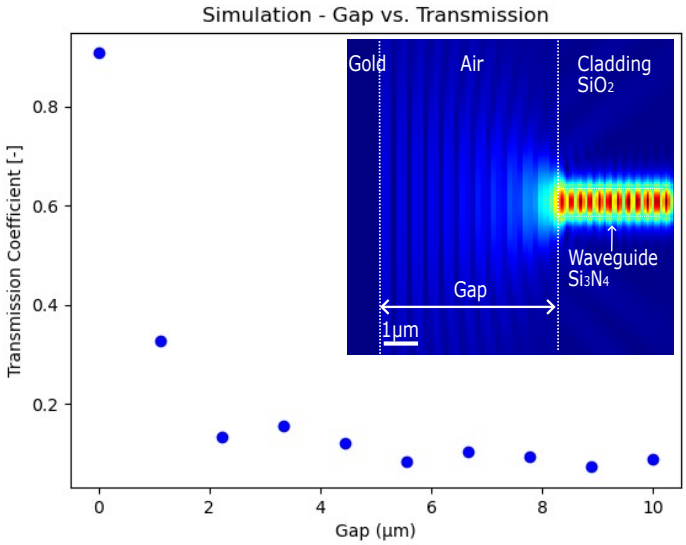

Figure 4.2: Normalized transmission, and thus coupling efficiency, as a function of the gap size.

In practice, the separation between the scanning sample and the waveguide sample varies between measurements and is estimated to be on the order of 10 μm, based on the field of view of the top camera. This estimate should be regarded as approximate due to the limited accuracy of this measurement method. For a wavelength of 881 nm, such distances place the system in the far-field regime.

Besides, it is not a priori evident that the mode launched into the waveguide remains identical to the mode coupled back after reflection, since reflections at a gold surface and across an air gap can introduce phase shifts or excite higher-order modes. Figure 4.3 compares the launched mode with the mode coupled back after reflection from a gold surface separated by a 5 μm air gap. The results show that the two modes remain very similar, indicating that under these conditions the back-coupling does not significantly distort the modal profile.

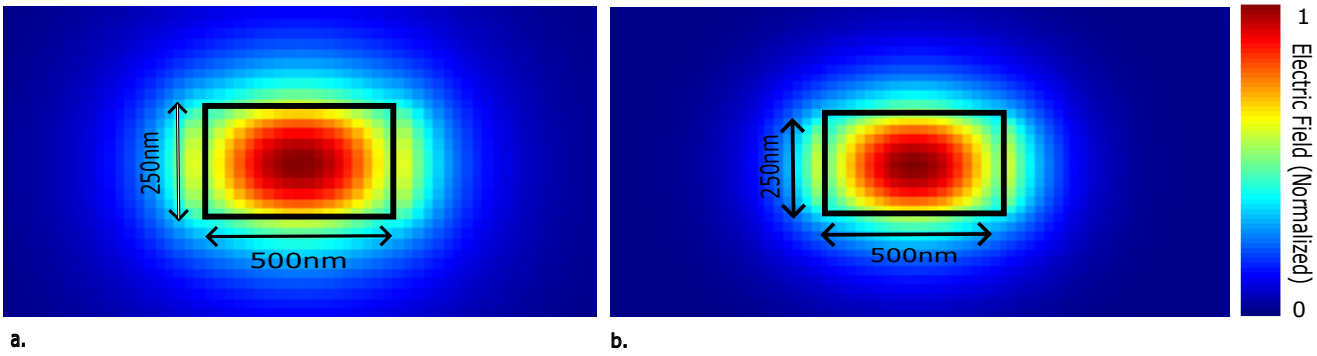

Figure 4.3: *a.* Mode launched into the waveguide. *b.* Mode after reflection from gold across a 5 μm air gap and coupled back into the waveguide. The similarity of the two profiles indicates that back-coupling does not substantially alter the modal shape in this configuration.

4.1.3. Waveguide Splitting

In the PIC system, light propagating in the reverse direction encounters the upper branch, which was originally used as the source. An abrupt Y-branch at this junction can induce reflections and mode distortion, reducing the fraction of light that continues straight back toward the photodetector.

To investigate this, an FDTD simulation was performed to analyze the transmission through each branch, using the same material and geometric parameters as the fully side-coupled waveguide design (see Section 3.2.2). In this design, the *lower branch* leads to the photodetector, so maximizing transmission through this branch is desirable. Figure 4.4 shows that widening the waveguide at the junction causes the electric field to split and the mode to expand.

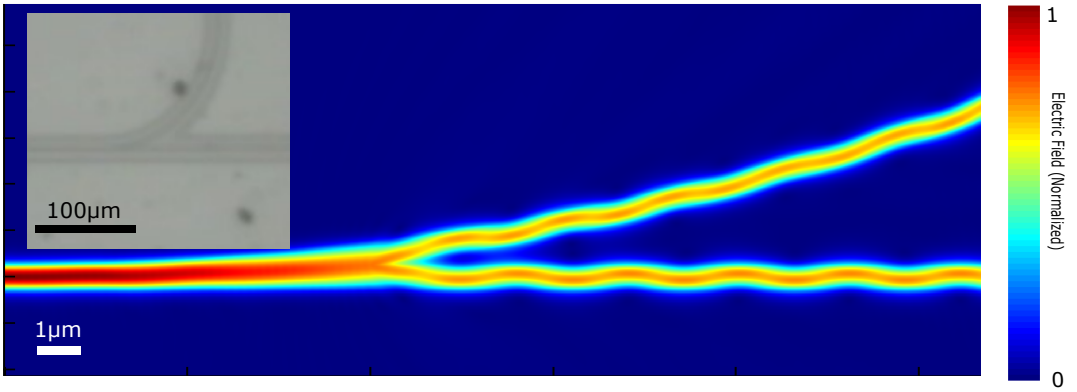

Figure 4.4: Electric field at the splitting point of the SiN waveguide.

Despite this expansion, the mode profile is largely preserved at the widest point. Simulations yield a distribution ratio of $T_{\text{lower branch}} : T_{\text{upper branch}} : T_{\text{loss}} = 0.512 : 0.487 : 0.001$, indicating that losses outside the waveguides are minimal under ideal circumstances, and a substantial fraction of light propagates toward the desired branch. The near-even distribution between the two branches suggests that the μ-shaped junction affects the splitting but does not significantly direct more light to the detector.

It is worth noting that in the literature, evenly splitting branches are often optimized by gradually widening the waveguide before the split, allowing the mode to expand and redistribute prior to the branching point [37, 38]. In this project, the focus is on maximizing transmission to a single branch rather than achieving equal splitting. Consequently, redesigning or optimizing the widening structures could improve the distribution.

4.1.4. Dark and Background Noise

Dark counts refer to detector counts occurring in the absence of any illumination and were found to be negligible. *Background counts* originate from ambient light and vary between scans; they can be measured by moving the imaging sample out of the optical path.

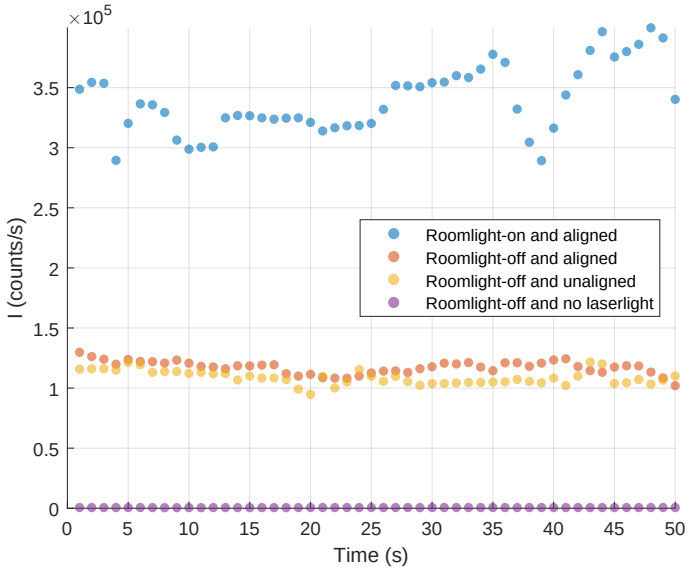

Figure 4.5: Normalized intensity versus time for four experimental conditions: aligned with laser (roomlight off), aligned with additional roomlight, unaligned in the dark, and no laser. A dashed line marks the mean intensity for the aligned, roomlight-off condition.

Figure 4.5 shows the intensity under different experimental conditions. Approximate average values were: aligned with roomlight on, $\sim 3.3 \times 10^5$ photoncounts per second; aligned with roomlight off, $\sim 1.2 \times 10^5$ counts/sec; unaligned in the dark, $\sim 1.1 \times 10^5$ counts/sec; and no laser, ~ 570 counts/sec. Both roomlight and the illumination stage increased the detected counts, highlighting the importance of switching these sources off during scans. The small difference between the intensity in "Roomlight-off and aligned" and "Roomlight-off and unaligned" indicates that the laser itself produces scattering within the detection system, contributing an additional signal unrelated to the sample.

Ideally, alignment ensures that the sample-generated signal dominates, providing high contrast when scanning, but this laser-induced scattering sets a significant baseline of detected intensity.

4.1.5. Grating Parameters

When it comes to the Grating Coupler-based waveguide sample, the grating parameters themselves are discussed: pitch, fill factor, and etch depth. To determine the optimal values for these parameters, optical simulations were performed using the finite-difference time-domain (FDTD) simulation software from ANSYS Lumerical.

Simulation Set-up

A single-mode source was injected into the waveguide. The simulations were performed in 2D along the longitudinal plane of the SiN waveguide (side view). The coupling efficiency was evaluated primarily at the position corresponding to the numerical aperture (NA) of the objective lens, NA = 0.75.

To assess the effective capture of light by the lens, a monitor is placed at a distance $y_{\text{mon}} = 30\ \mu$m above the grating coupler. This distance is shorter than the actual focal length of the lens for computational efficiency. To relate the monitor size to the field of view of the objective, the horizontal extent of the beam captured by the lens is defined as x_{NA} (i.e., the width of the field corresponding to the numerical aperture).

$$\theta = \arcsin(\text{NA}) = \arcsin(0.75) \approx 48.59^\circ, \tag{4.2}$$

Using but geometry, the horizontal field of view is given by

$$x_{\text{NA}} = 2\, y_{\text{mon}} \tan\theta \approx 2 \cdot 30\ \mu\text{m} \cdot \tan(48.59^\circ) \approx 68\ \mu\text{m}. \tag{4.3}$$

Period

A good starting point for designing the grating is to estimate its period based on the material parameters of the silicon dioxide (SiO_2) cladding and the SiN waveguide. For a half-filled grating, the effective refractive index can be approximated as $n_{\text{eff}} = (1-F)n_{\text{SiO}_2} + Fn_{\text{SiN}} = 0.5 \cdot 1.457138 + 0.5 \cdot 2.008032 = 1.733$, where $\lambda = 881$ nm and $F = 0.5$ is the fill factor. The light is intended to be diffracted upwards, and the fiber is typically angled (here, $\theta = 10°$) because vertical coupling ($\theta = 0°$) is inefficient due to low coupling efficiency and high back reflection. Substituting these parameters into the grating equation (Eq. 2.29) yields a grating period of $\Lambda = 595.5$ nm. A parameter sweep is performed around this value to evaluate the optimal transmission. In Fig. 4.6a, the red dot shows that a period of $\Lambda = 600$ nm lies at the center of a high-transmission plateau. This period is therefore selected for further use.

Fill-factor/Apodization

Normally, grating couplers are used to transfer a Gaussian-shaped beam of light into an optical fiber. Although in this case light does not need to be coupled into a fiber and mode matching is therefore not an issue, maintaining a Gaussian-like distribution may still improve performance. An increase in efficiency for an apodized grating is tested—that is, the fill factor is varied along the grating length. Specifically, the grating begins with a high fill factor (F_{start}) near the waveguide and gradually decreases toward the outer edge (F_{final}).

Working with a grating period of $\Lambda = 600$ nm, and setting the difference between F_{start} and F_{final} to $\Delta F = F_{\text{start}} - F_{\text{final}} = 0.4$, the results shown in Fig. 4.6b are obtained. The highest transmission value so far is indicated by a red dot and corresponds to $[F_{\text{start}}, F_{\text{final}}] = [0.7, 0.3]$.

Since light from the waveguide first encounters the portion of the grating with F_{start}, most of the radiation is emitted near the beginning of the grating coupler. It is therefore instructive to investigate, for the value of F_{start} considered earlier (0.7), the optimal value of F_{final}. This analysis is summarized in Fig. 4.6c, where the red point indicates that $[F_{\text{start}}, F_{\text{final}}] = [0.7, 0.45]$ achieves the highest transmission ($T = 0.21$) within this parameter range into the objective lens.

After fabrication of the PIC design, the analysis was repeated. Due to a systematic simulation error, the grating was fabricated with $[F_{\text{start}}, F_{\text{final}}] = [0.4, 0.1]$. For the intended design values (i.e., without the systematic simulation error), $[F_{\text{start}}, F_{\text{final}}] = [0.4, 0.1]$ results in a transmission of $T = 0.14$.

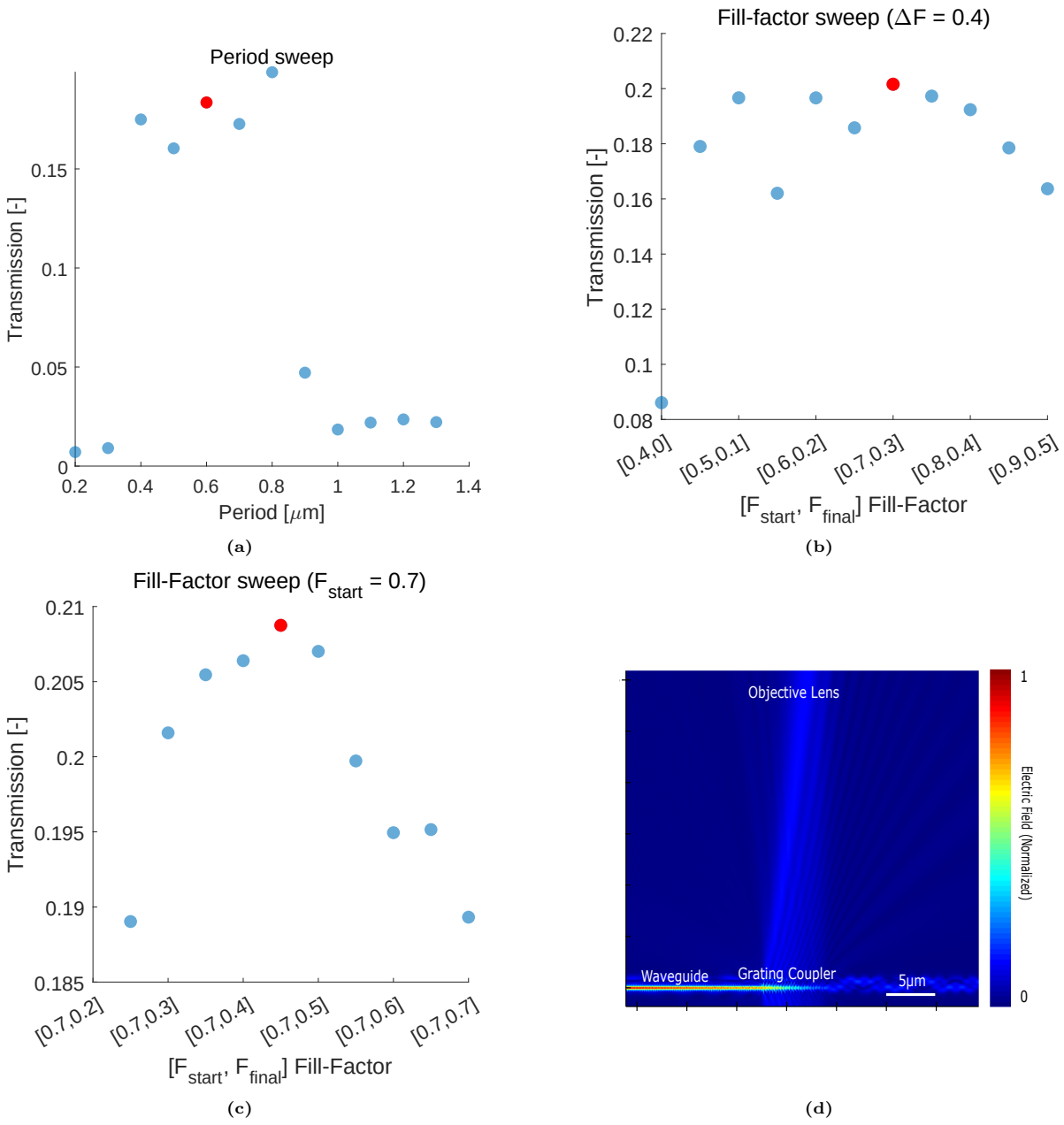

Figure 4.6: Sweep scans over the period and fill factors (a–c) led to a grating coupler with high transmission towards the objective lens. Panel (d) shows a side view of the electric field formed above the grating coupler.

4.2. Imaging Results

4.2.1. Discrete Fully-Side-Coupled Scans

The first sample investigated is shown in Fig. 4.7a. It is a useful test case for comparing contrast between two very different intensity regions. The LN region appears yellow, while the gold region looks dark. This is somewhat unexpected, since at the operating wavelength of $881,\mathrm{nm}$ the LN side should appear darker and the gold side brighter.

The scanned area covers a narrow boundary between the LN and gold regions. Red striped lines in the image show the position of this transition zone. The expected contrast from scanning across this boundary with SNOM is shown in Fig. 4.7b.

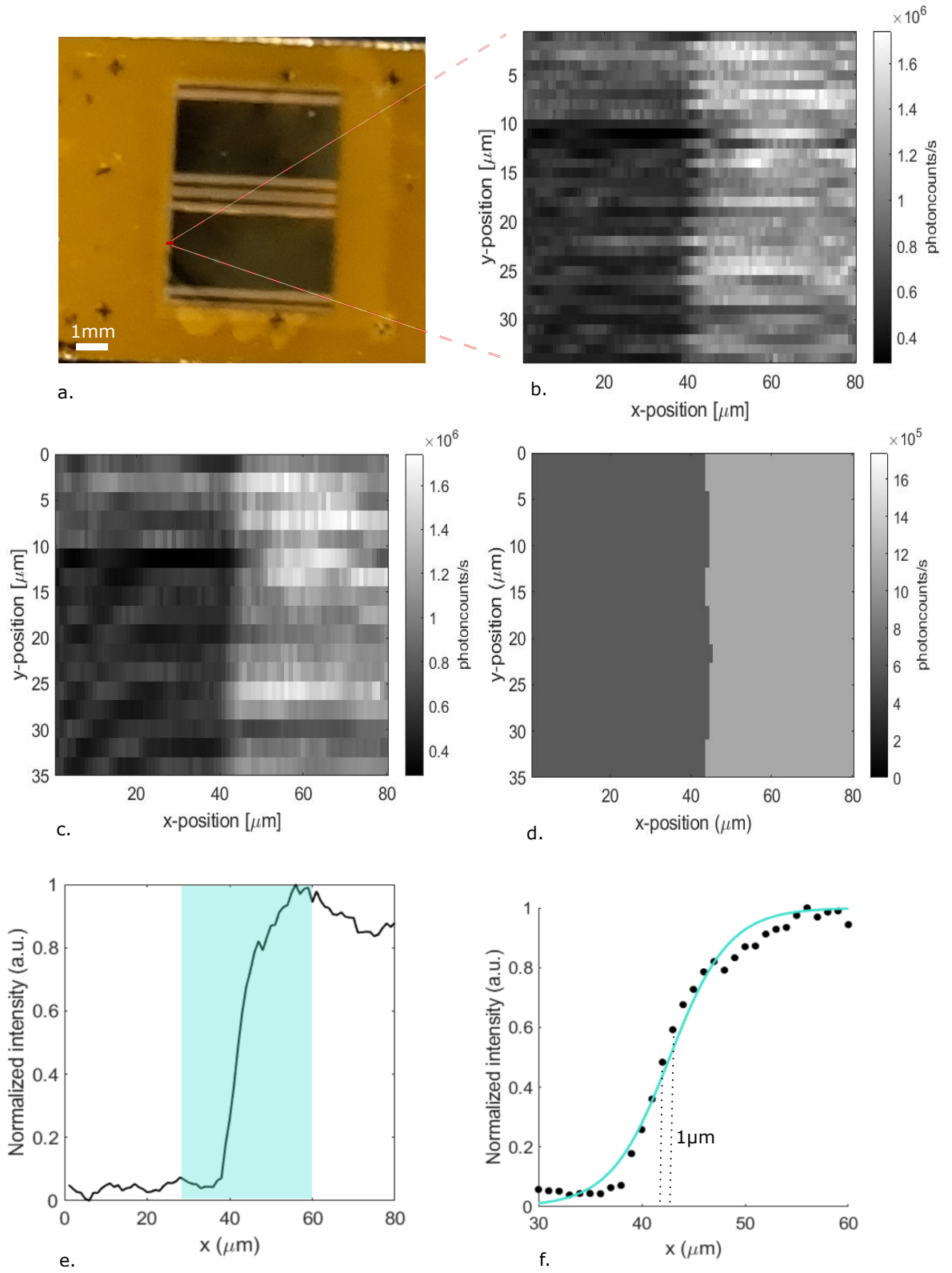

Figure 4.7: **a** Photograph of the imaging sample. **b** Scanning result over an area of $35 \times 80\,\mu m^2$. **c** Result after removing even lines, showing left-to-right scanning. **d** Post-processed result using an averaging filter to remove misaligned values and distinguish foreground from background. **e** Normalized average intensity across columns. **f** Normalized average intensity of the transition region (blue), demonstrating that distinct features can be resolved with a spatial resolution of $1\,\mu m$.

In Fig.4.7b, one can see that the odd lines appear shifted compared to the even lines, resulting in a jagged transition line. This occurs because the odd lines were scanned during the left-to-right movement of the closed-loop piezomotor, while the even lines were scanned in the opposite direction. The step sizes differ between these two directions. Fig.4.7c shows the result after removing the even lines, effectively producing a one-sided raster scan.

Post-processing can be taken a step further by noting that only two materials are present on the sample surface. Consequently, only two intensity levels are required: one for reflective gold and one for the transmitting Lithium Niobate ($I_{background}$). Fig. 4.7d shows the thresholded result. Here, the average intensity of a neighborhood of eight connected pixels around each pixel, including the pixel itself, is compared to the average intensity of the full image ($\bar{I}_{\text{global}}$). A pixel is classified as foreground only if this local average exceeds $\bar{I}_{\text{global}}$, in which case it is assigned the average foreground intensity. Otherwise, it is assigned the average background intensity. In formula form:

$$I_{\text{out}}(p) = \begin{cases} \bar{I}_{\text{foreground}}, & \text{if } \frac{1}{|N_8(p)\cup\{p\}|}\sum_{q\in N_8(p)\cup\{p\}} I(q) > \bar{I}_{\text{global}}, \\ \bar{I}_{\text{background}}, & \text{otherwise,} \end{cases} \qquad \forall p \in \Omega \tag{4.4}$$

In this equation, p denotes a pixel in the image domain Ω, $I(q)$ is the original intensity of pixel q, and $N_8(p) \cup \{p\}$ represents the 8-connected neighbors of p including p itself.

Fig. 4.7e shows the average intensity value of each column of the left-to right scan (Fig. Fig. 4.7c). The values are normalized setting the lowest value to 0 and the highest to 1. By analyzing the transition between the dark and the bright region, shown in Fig. 4.7f, the spatial resolution of the system is determined to be approximately 1 μm.

Several metrics can be used to quantify contrast. The Michelson contrast is commonly employed for patterns with bright and dark features [39], and is defined as:

$$contrast = \frac{L_{\text{foreground}} - L_{\text{background}}}{L_{\text{foreground}} + L_{\text{background}}}, \tag{4.5}$$

where L denotes the luminance. Here, we substitute L with the average intensity values measured by the APD (in counts per second). Using this substitution, the contrast between foreground and background is 0.30, or 30%.

Rather than a simple gradient from dark to light, a structured sample containing lines of varying widths was studied, as shown in Fig. 4.8a. The corresponding measurement produced a two-sided raster scan, Fig. 4.8b, from which a one-sided raster scan was obtained by removing the even lines, Fig. 4.8c.

The figures show that the data is affected by an oscillating background noise, most likely originating from Fabry–Pérot interference within the sample. To suppress this effect, the Fast Fourier transform of the image was computed and the high spatial frequencies were attenuated in the Fourier domain. Rather than applying a hard cut-off, which tends to introduce artifacts such as ringing, a smooth Gaussian mask was used. The mask has the functional form

$$G(x, y) = \exp\left[-\frac{(x - x_0)^2 + (y - y_0)^2}{2\sigma^2}\right],$$

where (x_0, y_0) denotes the center of the Fourier plane and σ controls the filter width. In this work we chose $\sigma = 10$ pixels, which provided sufficient suppression of high-frequency noise while preserving the structural features of the sample. In this way, low-frequency components at the center are preserved while higher spatial frequencies are gradually suppressed.

The filtered Fourier spectrum is shown in Fig. 4.8d. After inverse transformation, the resulting image (Fig. 4.8e) is noticeably smoother, with the main structural features preserved and the Fabry–Pérot oscillations largely removed. Finally, Fig. 4.8f shows the application of a thresholding filter, obtained in a similar fashion as Fig. 4.7d, clearly separating foreground and background, thereby distinguishing the two different materials. The Michelson contrast of this result is 0.20.

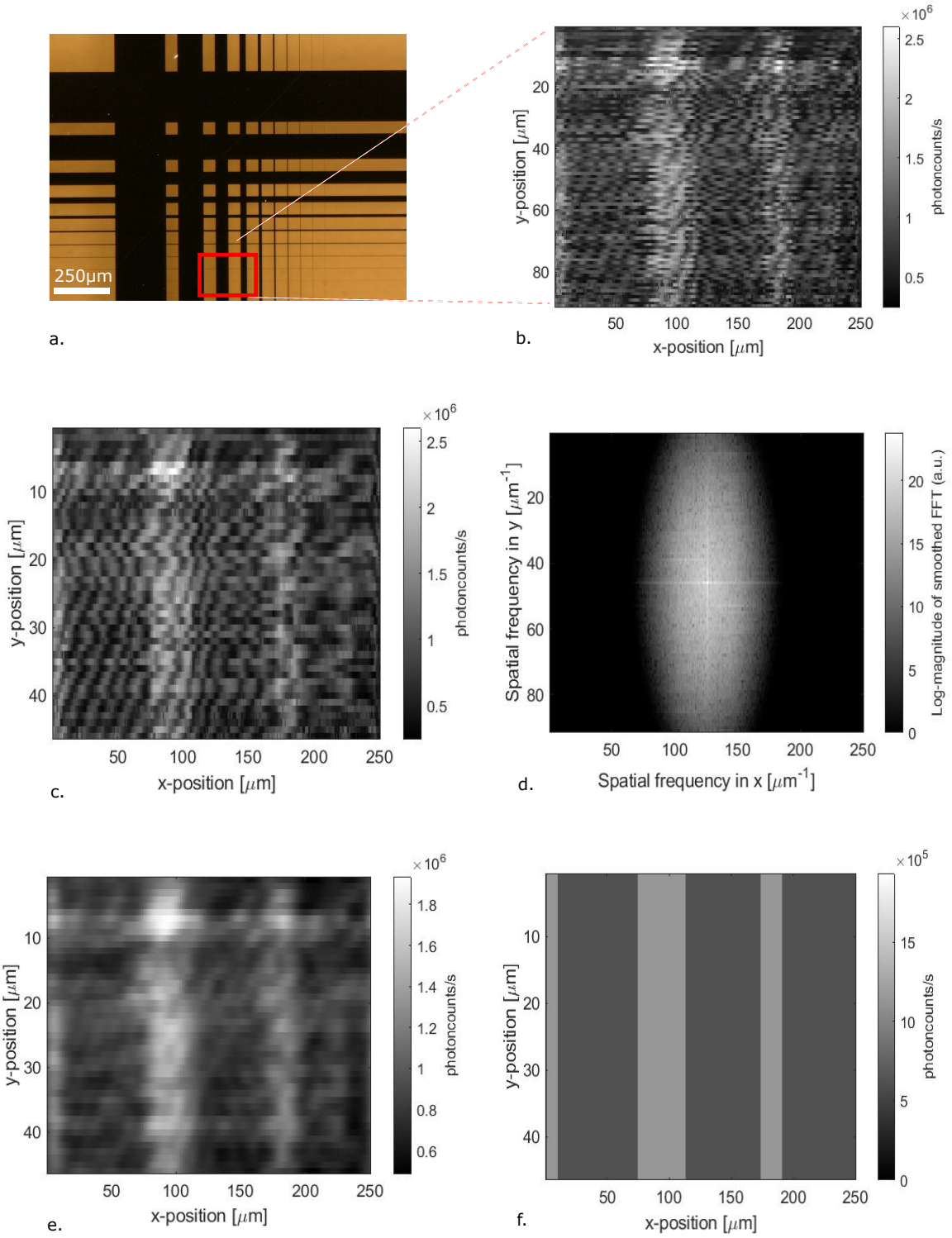

Figure 4.8: **a.** SEM image of a sample fragment. **b.** Back and forth raster scan of the segment. **c.** Left-to right scan. **d.** Fourier domain, with erased high spatial frequencies. **e.** Inverse Fourier Transformed result. **f.** Complete fore en background removal using thresholding.

4.2.2. Continuous Fully-Side-Coupled Scans

A continuous scanning technique was employed, in which scanning occurs simultaneously with motor movement, rather than using a discrete move-and-scan approach. This method was applied to a sample containing 100 μm-wide gold lines as the foreground and lithium niobate as the background at a wavelength of $\lambda = 881$ nm (see Fig. 4.9a).

For microscopy, focus was placed on a 90° edge of the pattern (see Fig. 4.9b). The piezo motors were programmed to acquire a 50×50 image with a scan resolution of 2 μm. Continuous scanning was performed with a piezo motor velocity of 250 steps/s, with each piezo-step corresponding to a claimed 52.9 nm [30]. The motors were only instructed to pause when moving to a new row. The total scanning time was measured using MATLAB to be 21 minutes and 28 seconds, compared to 45 minutes and 23 seconds for a discrete scan of the exactly same format.

Fig. 4.9d shows the thresholded image used to distinguish the foreground from the background, based on eq. 4.4. Thresholding was performed by evaluating, for each pixel, whether the average intensity within its 9×9 neighborhood was above or below the mean overall intensity. The Michelson contrast is 0.19.

Figures 4.9e and f assess the continuity of the transition between bright and dark regions, providing an indication of the imaging resolution.

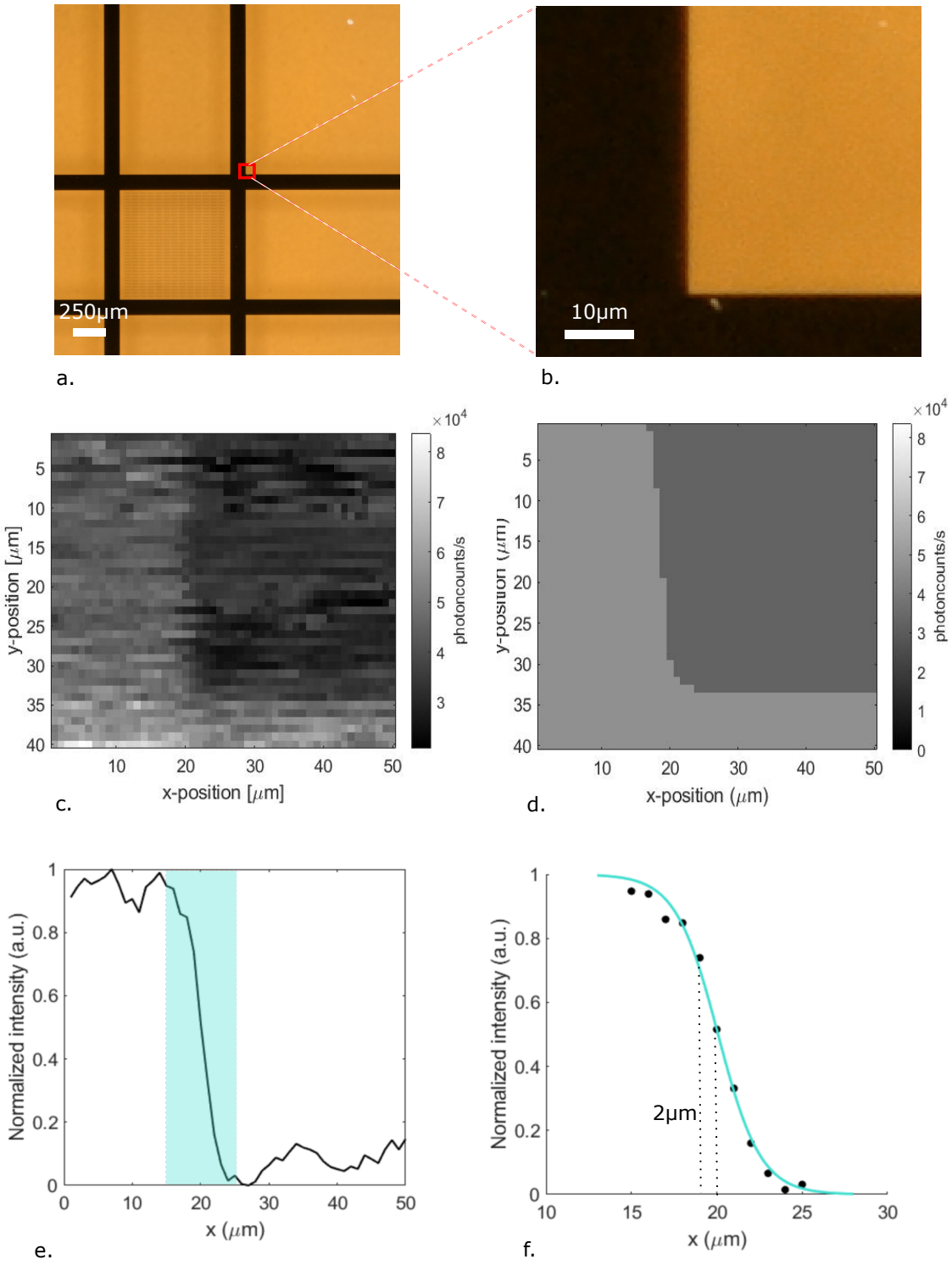

Figure 4.9: a. SEM image of the imaging sample. **b.** Section of interest. **c.** Scanning result. **d.** Thresholded fore- and background. **e.** Normalized average intensity across the full width (columns). **f.** Normalized average intensity of the transition part

, shown in blue in c. Here, distinct features can be resolved with a spatial resolution of 2 μm.

4.2.3. Grating-Coupler-Integrated Scans

The grating-coupler-based PIC sample was scanned along a single spatial dimension (1D), say x, which simplifies coverage over large distances due to the lack of automated scanning. However, the sample was not cleaved straightly, complicating efforts to minimize scattering and making close-proximity measurements more challenging.

Figure 4.10a highlights the specific region of the sample targeted for imaging. A reflective gold line, 250 μm wide, is present on the sample.

As shown in Appendix B, the waveguide structure on the PIC sample splits into four branches. For this scan, a design with parallel waveguide branches separated by $\Delta x = 128$ μm was used. Each branch was scanned over a distance of 150 μm, slightly exceeding the branch separation to ensure complete coverage. The four branches were individually scanned over a total range of 600 μm with a scanning resolution of 1 μm. By combining data from all four branches, a composite scan across the entire 250 μm-wide gold line was reconstructed, as shown in Fig. 4.10b.

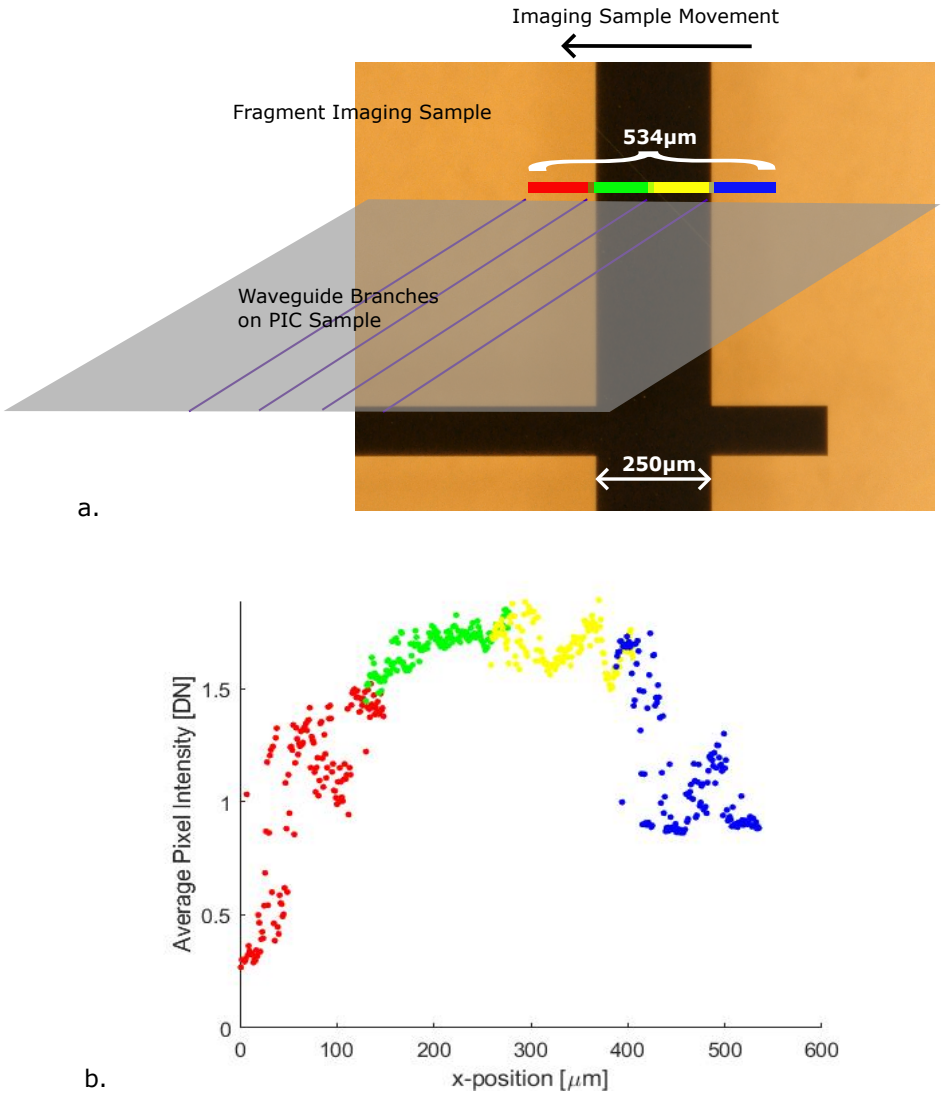

Figure 4.10: (a) SEM image of the imaging sample. The colours represent the data from each of the four waveguidebranches connected each to a grating coupler. (b) 1D scanning result across the 250μm wide line, using the grating-coupler-integrated waveguide. The bright colors represent the data from the individual branches

The observed contrast appears to vary depending on the specific branch containing the grating coupler. To quantify this variation, the foreground and background intensity levels along each branch are identified using the first and last measured values.
For the first branch, the intensity rises from a background level of 0.27 to a foreground level of 1.38, resulting in a contrast of $C = (1.38 - 0.27)/(1.38 + 0.27) \approx 0.67$. In the fourth branch, the intensity decreases from a foreground level of 1.04 to a background level of 0.33, giving a contrast of $C = (1.04 - 0.33)/(1.04 + 0.33) \approx 0.52$.

5

Discussion and Conclusion

5.1. Discussion

Experimental Setup and Sample Design
When comparing different *material choices* of the image samples, significant performance differences were observed. Tests using the initial silicon imaging sample showed low contrast and no images were obtained in this project, whereas the silicon nitride sample provided noticeably better contrast.

For the silicon sample, the reduced performance may be attributed to the presence of a silicon dioxide layer on top of the silicon, which can increase reflectivity. This oxide layer is typically formed during the production process as silicon reacts with oxygen at elevated temperatures. Oxygen can diffuse into silicon during thermal processing, leading to the formation of a thermally grown silicon dioxide layer.

Horizontal lines in the *imaging sample pattern* proved effective for spatial recognition of 2D structures. In previous image designs, it was difficult to identify features due to the lack of recognizable reference points. Using *repetitive* text, such as the "TU Delft" pattern, addressed this issue by providing a consistent and identifiable reference across the sample. However, the individual letters, with a thickness of 0.8 μm, were still challenging to resolve reliably. This limitation underscores the need for patterns that balance recognizability with feature size to convey meaningful spatial information.

Experimentally, a 1 μm step size proved sufficient to generate contrast in the *grating-coupler-based system*, comparable to that of a fully side-coupled configuration. However, the grating-coupler sample was not cleaved perfectly straight, preventing the maintenance of a small and uniform air gap during scanning. This uneven cleaving introduced additional scattering, potentially resulting in flickering intensity during 1D scans.
Despite these limitations, clear contrast was achieved at a similar resolution, while the challenges associated with unstable double side-coupling were avoided. The signal showed fluctuations which may be solved with more simulation analysis and better grating parameters. Moreover, splitting up the waveguide in four branches was successfully realized, yielding higher sampling density and indicating potential for faster scanning.

There is considerable variation in the *coupling technique* between the optical fiber and the waveguide entrance. In this experiment, side coupling was used to insert light, and its effectiveness was primarily assessed by monitoring the photon counts returned to the APD and by observing scattering on a single camera view. These indicators provided guidance but were not fully reliable for identifying the optimal side-coupling position. A more stable coupling method, or the addition of an auxiliary visualization stage, could help reduce this uncertainty.

The resolution and precision of the imaging are fundamentally limited by the *beam spot size*. Using reflective materials and advanced waveguide designs, light can be focused to spots only a few nanometers in diameter, thereby enhancing resolution [40, 41]. In the present work, however, priority was given to

stability and reproducibility, which placed constraints on the achievable imaging performance. Moreover, the fabrication of such advanced structures is considerably more complex. As the project progresses, the implementation of focusing waveguide structures should be considered to further improve resolution. Furthermore, it may be advisable to replace the tapered fiber. Although light is still coupled into the waveguide, the fiber tip has likely lost its sharpness, which may result in increased scattering and higher losses.

Measurement Considerations
Microscopy images were acquired at twice the speed using the continuous *scanning method* compared to the conventional stepwise (discrete) approach. In principle, the acquisition rate could be increased by up to a factor of 16 (from 13.225 μm/s to 105.800 μm/s), which is the maximum speed of the closed-loop piezomotor [42], provided that photodetection is accurately synchronized with the motor motion through precise computer control.

A procedure was developed to minimize the air gap between the waveguide and the sample, but this gap remains on the order of microns and is therefore still in the far field. For near-field effects, the separation would need to be $r \lesssim 100$ nm from the waveguide. The overall width of the PIC waveguide sample presents an additional challenge when attempting to operate within the near-field regime.

In the fully side-coupled version of the PIC-based microscopy, light is often observed to scatter directly from the inserting fiber to the nearby collecting fiber without passing through the PIC sample. A double side-coupled configuration may still function adequately, whether grating couplers or optical fibers are used. However, the collection stage should be positioned separately from the inserting fiber, preferably along a different edge of the PIC sample, to minimize unintended scattering.

Future Perspective
The concept of waveguide-based SNOM shows strong potential for achieving high-contrast and stable imaging results. Over time, it became evident that identifying and mitigating sources of instability is crucial. In particular, the imaging sample stage (Fig. 3.14) would benefit from increased stiffness. A redesign is recommended to reduce the extent to which the sample extends beyond its center of mass.

In addition, noise analysis indicates that it would be advantageous to move permanently beyond the fully side-coupled design toward configurations where the collecting branch is not placed directly beside the inserting branch. The grating-coupler-based design represents a promising candidate for this purpose and warrants further investigation. Future work should explore smaller separation distances between the four waveguide branches, as well as implementing automated raster scanning to enable full 2D imaging rather than limiting acquisition to 1D line scans.

For improved stability, one option is to retain side coupling while integrating an additional collection stage on a different edge of the PIC sample. A permanent fiber-to-waveguide connection could further reduce instability, although this approach may be more practical to pursue in future work.

5.2. Conclusion

In this project, careful design of the waveguide parameters is crucial for waveguide-based scanning near-field optical microscopy (SNOM). Simulations indicated that SiN waveguides with a 500×250, nm cross-section embedded in SiO_2 maintain single-mode operation. A fully side-coupled, waveguide-based microscopy setup is employed, in which both the input and collection fibers couple laterally to waveguide branches. This configuration achieved a spatial resolution of 1 μm. Continuous scanning effectively doubled the acquisition speed, enabling a 50×50 pixel image to be acquired in 21 minutes and 28 seconds, with a Michelson contrast of approximately 0.3. With respect to the *research question* posed in Section 1.2, the primary technical challenges concern signal stability. Analysis shows that the signal can be stabilized by using an attenuator and maintaining a generated current of 10 mA. In addition, approximately 90% of the light from the input fiber was directly scattered into the detection fiber. Another issue observed with the fully side-coupled PIC sample is that it can become completely misaligned within 20 seconds. To address these challenges, a proof-of-concept PIC design was developed using grating couplers for detection instead of an additional optical fiber, thereby avoiding scattering losses. Simulations indicate that an apodized grating with a fill factor decreasing from 0.7 at the base to 0.45 at the end achieves a transmission of $T = 0.21$ at the objective lens, which provides improved visibility. With the grating couplers serving as the detection system, a one-dimensional scan across 512 μm with 1 μm resolution demonstrated that the design can cover larger areas by splitting the waveguide into four branches, while also reducing the instability issues associated with side coupling. This approach further improved the Michelson contrast to approximately 0.6, compared to 0.3 in the previous setup.

5.3. Acknowledgments

Firstly, I would like to express my sincere gratitude to my project supervisor, Dr. Iman Esmaeil Zadeh, for his guidance, inspiring motivation to pursue research, as well as for introducing me to such an exciting project.

I am deeply thankful to my daily supervisors, Zizheng and Naresh, for their dedication, motivation, and constant care for the progress of the work.

My sincere appreciation goes to the technical staff, in particular Thomas, whose practical expertise and enthusiasm made the design process both insightful and enjoyable.

This project has been a collaborative effort, and I would like to thank the entire research group for their openness to brainstorming and their willingness to offer help whenever needed.

Ik ben ook alle medestudenten in het studentenkantoor dankbaar voor de brainstormsessies, de vele gedeelde momenten van plezier en de ondersteunende sfeer waarin we elkaar door uitdagingen heen hebben geholpen. Jaap, Freek en Hugo, ik heb genoten van de conferenties en de verhelderende recreatieve activiteiten.

Tijdens dit project heeft mijn vriendin Anne mij enorm gesteund en veel rust gegeven. Bedankt.

References

[1] Serge Valette. "Integrated Optics: The History and the Future". In: *Proceedings of the European Conference on Integrated Optics (ECIO 2007)*. Plenary talk; CEA-LITEN, France. 2007.

[2] Gyungseok Oh, Euiheon Chung, and Seok H. Yun. "Optical fibers for high-resolution in vivo microendoscopic fluorescence imaging". In: *Optical Fiber Technology* 19.6, Part B (2013). Optical Fiber Sensors, pp. 760–771. ISSN: 1068-5200. DOI: https://doi.org/10.1016/j.yofte.2013.07.008. URL: https://www.sciencedirect.com/science/article/pii/S1068520013000886.

[3] Paul Bazylewski, Sabastine Ezugwu, and Giovanni Fanchini. "A Review of Three-Dimensional Scanning Near-Field Optical Microscopy (3D-SNOM) and Its Applications in Nanoscale Light Management". In: *Applied Sciences* 7.10 (2017), p. 973. DOI: 10.3390/app7100973.

[4] Qiaosheng Pan et al. "Development of a novel resonant piezoelectric motor using parallel moving gears mechanism". In: *Mechatronics* 98 (2023), p. 103097. DOI: 10.1016/j.mechatronics.2023.103097. URL: https://www.sciencedirect.com/science/article/pii/S0957415823001538.

[5] Oxford Instruments (WITec). *Scanning Near-field Optical Microscopy (SNOM)*. https://raman.oxinst.com/techniques/snom. Accessed: YYYY-MM-DD. 2025.

[6] Georg Rademacher et al. "Peta-bit-per-second optical communications system using a standard cladding diameter 15-mode fiber". In: *Nature Communications* 12.1 (2021), p. 4238. DOI: 10.1038/s41467-021-24409-w. URL: https://www.nature.com/articles/s41467-021-24409-w.

[7] Robert G. Hunsperger. *Integrated Optics: Theory and Technology*. 6th ed. Advanced Texts in Physics. Originally published in the series: Advanced Texts in Physics. Springer New York, NY, 2009, pp. XXVIII, 513. ISBN: 978-0-387-89774-5. DOI: 10.1007/b98730. URL: https://doi.org/10.1007/b98730.

[8] Larry A. Coldren, Scott W. Corzine, and Milan Mashanovitch. *Diode Lasers and Photonic Integrated Circuits*. English. 2nd. Hoboken, N.J.: Wiley, 2012. ISBN: 9781118148198, 1118148193, 9781118148167, 1118148169, 9786613618047, 6613618047, 1280588217, 9781280588211, 1118148185, 9781118148181.

[9] Daniel Pérez et al. "Multipurpose silicon photonics signal processor core". In: *Nature Communications* 8 (2017), p. 636. DOI: 10.1038/s41467-017-00714-1. URL: https://www.nature.com/articles/s41467-017-00714-1.

[10] Christoforos Kachris, Konstantinos Kanonakis, and Ioannis Tomkos. "Optical interconnection networks in data centers: recent trends and future challenges". In: *IEEE Communications Magazine* 51.9 (2013), pp. 39–45. DOI: 10.1109/MCOM.2013.6588648.

[11] J. Hecht. "Lidar for Self-Driving Cars". In: *Optics & Photonics News* 29.1 (2018), pp. 26–33. DOI: 10.1364/OPN.29.1.000026.

[12] H. Majeed et al. "Quantitative phase imaging for medical diagnosis". In: *Journal of Biophotonics* 10 (2017), pp. 177–205. DOI: 10.1002/jbio.201600113. URL: https://onlinelibrary.wiley.com/doi/10.1002/jbio.201600113.

[13] Karan K. Mehta et al. "Integrated optical multi-ion quantum logic". In: *Nature* 586.7830 (Oct. 2020), pp. 533–537. ISSN: 1476-4687. DOI: 10.1038/s41586-020-2823-6. URL: http://dx.doi.org/10.1038/s41586-020-2823-6.

[14] R. Diekmann et al. "Chip-based wide field-of-view nanoscopy". In: *Nature Photonics* 11 (2017), pp. 322–328. DOI: 10.1038/nphoton.2017.55. URL: https://www.nature.com/articles/nphoton.2017.55.

[15] Øystein I. Helle et al. "Nanoscopy on-a-chip: super-resolution imaging on the millimeter scale". In: *Optics Express* 27.5 (2019), pp. 6700–6710. DOI: 10.1364/OE.27.006700. URL: https://pubmed.ncbi.nlm.nih.gov/30876250/.

[16] Songlin Yang et al. “Waveguide-based microscope slide for label-free high-resolution imaging”. In: *Applied Physics Letters* (2024). URL: https://api.semanticscholar.org/CorpusID:271732638.

[17] Gangwei Jiang et al. “A synergistic strategy to develop photostable and bright dyes with long Stokes shift for nanoscopy”. In: *Nature Communications* 13 (2022). DOI: 10.1038/s41467-022-29547-3. URL: https://www.nature.com/articles/s41467-022-29547-3.

[18] Nikhil Jayakumar et al. “Multi-moded high-index contrast optical waveguide for super-contrast high-resolution label-free microscopy”. In: *Nanophotonics* 11.15 (2022), pp. 3421–3436. DOI: 10.1515/nanoph-2022-0100.

[19] David J. Hill et al. “Waveguide Scattering Microscopy for Dark-Field Imaging and Spectroscopy of Photonic Nanostructures”. In: *ACS Photonics* 1.10 (2014), pp. 1077–1085. DOI: 10.1021/ph5001617.

[20] Björn Agnarsson et al. “Evanescent Light-Scattering Microscopy for Label-Free Interfacial Imaging: From Single Sub-100 nm Vesicles to Live Cells”. In: *ACS Nano* 9.12 (2015), pp. 11849–11862. DOI: 10.1021/acsnano.5b04168.

[21] Jean Terrien and André Maréchal. *Optique théorique*. French. Que sais-je? 615. Paris: Presses Universitaires de France, 1954.

[22] David J. Griffiths. *Introduction to Electrodynamics*. 4th ed. Cambridge University Press, 2017.

[23] A.P. (Sander) Konijnenberg. *Lecture Notes: Basic Optics, Fourier Optics*. Unpublished manuscript. Lecture notes, email: a.p.konijnenberg@gmail.com. Sept. 2023.

[24] M. N. Berberan-Santos. “Beer’s Law Revisited”. In: *Journal of Chemical Education* 67.9 (1990), p. 757. DOI: 10.1021/ed067p757.

[25] Eugene Hecht. *Optics Global Edition*. Pearson Deutschland, 2016, p. 728. ISBN: 9781292096933. URL: https://elibrary.pearson.de/book/99.150005/9781292096964.

[26] Li Long et al. “3D printing of plasmonic nanofocusing tip enabling high resolution, high throughput and high contrast optical near-field imaging”. In: *Light: Science & Applications* 12 (2023). Official journal of the CIOMP, Open Access, ISSN 2047-7538, p. 219. DOI: 10.1038/s41377-023-01272-6. URL: https://www.nature.com/lsa.

[27] Zhexin Zhao and Shanhui Fan. “Design Principles of Apodized Grating Couplers”. In: *J. Lightwave Technol.* 38.16 (Aug. 2020), pp. 4435–4446. URL: https://opg.optica.org/jlt/abstract.cfm?URI=jlt-38-16-4435.

[28] Gyeongho Son et al. “High-efficiency broadband light coupling between optical fibers and photonic integrated circuits”. In: *Nanophotonics* 7.12 (2018), pp. 1845–1864. DOI: 10.1515/nanoph-2018-0069.

[29] OZ Optics. *V-Groove Assemblies*. 2016. URL: https://www.ozoptics.com/ALLNEW_PDF/DTS0083.pdf.

[30] Newport. *Picomotor – Open vs. Closed Loop*. English. Newport. 2020. 4 pp.

[31] S. E. Miller. “Integrated Optics: An Introduction”. In: *Bell System Technical Journal* 43.6 (1964), pp. 1727–1739.

[32] Francesco Ceccarelli et al. “Recent advances and future perspectives of single-photon avalanche diodes for quantum photonics applications”. In: *Advanced Quantum Technologies* 4.10 (2021), p. 2000102. DOI: 10.1002/qute.202000102.

[33] Excelitas Technologies. *SPCM-AQRH Series Single Photon Counting Module User Manual*. Version Rev 2023-1. Excelitas Technologies. Vaudreuil-Dorion, Quebec, Canada, 2023. URL: https://www.excelitas.com/file-download/download/public/103899?filename=SPCM_User_Manual.pdf.

[34] Yue Zhou et al. “A low loss silicon waveguide bend based on width and curvature variations”. In: *Optics Communications* 565 (2024), p. 130679. ISSN: 0030-4018. DOI: https://doi.org/10.1016/j.optcom.2024.130679. URL: https://www.sciencedirect.com/science/article/pii/S0030401824004164.

[35] T. Sun and M. Xia. “Low loss modified Bézier bend waveguide”. In: *Optics Express* 30.7 (Mar. 2022), pp. 10293–10305. DOI: 10.1364/OE.452580.

[36] Herman M.J.R. Soemers. *Design principles for precision mechanisms*. English. Netherlands: University of Twente, 2010. ISBN: 978-90-365-3103-0.

[37] Yohei Sakamaki et al. “Low-Loss Y-Branch Waveguides Designed by Wavefront Matching Method”. In: *J. Lightwave Technol.* 27.9 (May 2009), pp. 1128–1134. URL: https://opg.optica.org/jlt/abstract.cfm?URI=jlt-27-9-1128.

[38] Pengfei Wang et al. “Design of an extra-low-loss broadband Y-branch waveguide splitter based on a tapered MMI structure”. In: *30th Progress in Electromagnetics Research Symposium (PIERS 2011) (12/09/11 - 16/09/11)*. 2011. URL: https://eprints.soton.ac.uk/341349/.

[39] Christiane B. Wiebel, Manish Singh, and Marianne Maertens. “Testing the role of Michelson contrast for the perception of surface lightness”. In: *Journal of Vision* 16.11 (Sept. 2016), p. 17. DOI: 10.1167/16.11.17. URL: https://doi.org/10.1167/16.11.17.

[40] Marcus Woo. *Nanodevice Can Focus Light into a Point Just a Few Billionths of a Meter Across*. Accessed: 2025-04-24. Dec. 2012. URL: https://scitechdaily.com/nanodevice-can-focus-light-into-a-point-just-a-few-billionths-of-a-meter-across/.

[41] Hyuck Choo et al. “Nanofocusing in a metal–insulator–metal gap plasmon waveguide with a three-dimensional linear taper”. In: *Nature Photonics* 6 (2012), pp. 838–844. DOI: 10.1038/nphoton.2012.277. URL: https://www.nature.com/articles/nphoton.2012.277.

[42] Newport Corporation. *Newport Closed-Loop Picomotor 8310CE User Manual*. User Manual. 2025. URL: https://www.newport.com/medias/sys_master/images/images/h7e/h3c/9642206068766/8310CE-User-Manual.pdf.

A

Alignment Steps

The coordinate axes used throughout the alignment process are defined in Figure A.1.

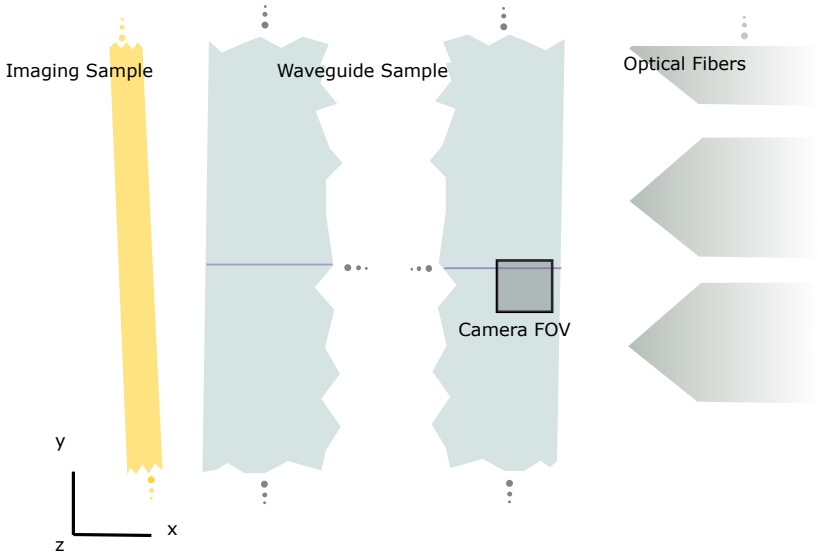

Figure A.1: Misaligned PIC imaging setup, where the components are rotated and the optical fiber is not side-coupled into the waveguide. The schematic and axis definitions support understanding of the alignment procedure.

Over time, a precise step-by-step procedure was developed to accurately align the PIC assembly. This careful and systematic approach was necessary because not every positioning stage provided all required degrees of freedom, and several components are mechanically fragile. In particular, improper handling can easily damage the waveguide when brought into contact with the optical fiber. Table A.1 shows the general alignment procedure before scanning to obtain an image.

In case that the PIC and image sample are replaced there are more steps to check on forehand. This is shown in table A.2.

Table A.1: *Alignment procedure before scanning.* Step-by-step alignment procedure for preparing the PIC setup before scanning. The optical fibers, waveguide sample, and imaging sample should already be mounted in their respective holders.

Step	Description
1	*Check and adjust the positions* of the imaging sample, waveguide sample and optical fibers, so that they are within the camera's field of view. The camera translation range is limited, so all elements must start within its travel range.
2	*Coarsely position* the optical fibers and the waveguide sample so that they are in proximity of each other.
3	*Rotate the PIC sample* until it is as parallel as possible to the vertical axis of the camera image. To verify this, move the imaging sample in different directions and check whether its position relative to the camera's field of view remains consistent.
4	*Rotate the imaging sample* similarly until it is as parallel as possible to the waveguide sample reducing Fabry-Pérot.
5	*Turn imaging sample away* from the waveguide sample for now.
6	Return to the coupling side and *move the optical fibers closer* to the waveguide facet, maintaining coarse alignment.
7	On the imaging side, *check the gap between the imaging sample and the PIC sample* by moving the camera up and down (z-axis). Adjust until the gap width remains constant across the field of view, indicating parallel alignment.
8	*Bring the optical fiber array* into its estimated position for side-coupling with the waveguide input facet.
9	Observe the waveguide output on the camera and *adjust the fiber positions* with the piezomotors until maximum output intensity is visible.
10	*Move the imaging sample closely* to the waveguide sample without making physical contact.
11	Fine-tune the fiber position by *monitoring the signal from the photodetector or grating couplers*, adjusting for maximum visible relfected light, or for maximum count rate. (These are not necessarily similar)
12	*check for oscillating Fabry–Pérot interference effects* using the motors at the imaging sample. If observed, slightly rotate the imaging sample to minimize them.
13	*Adjust light power to the stable regime.*
14	*Switch all lights off.*

Table A.2: Alignment procedure after positioning samples

Step	Description
1	*Reposition the stages* so they are approximately within the range of the camera movement, ensuring coverage of the entire PIC surface.
2	*Align the stages with each other* using the reference markers on the optical table.
3	*Repeat steps 1 and 2 until proper alignment is achieved.*
4	*Verify focus consistency along the x-direction (see Fig. A.1)* by moving the objective (camera FOV) across the PIC surface. Adjust tilt until focus remains constant, indicating minimal tilt.
5	*Check for residual tilt along the y-direction.*

B

Details Sample Design

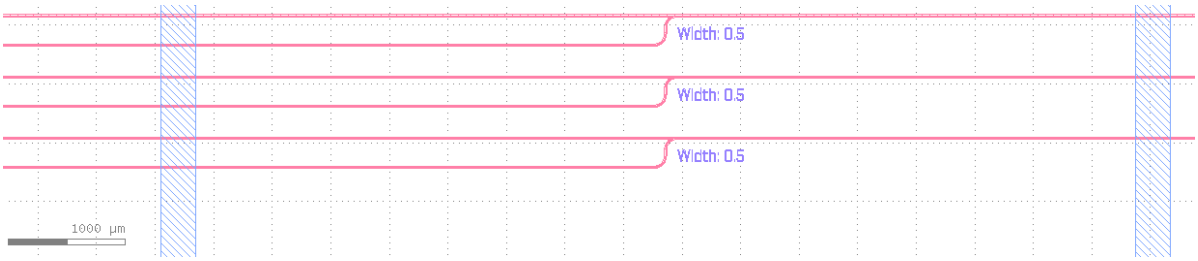

Figure B.1: Layout of three fully side-coupled waveguides integrated on a single chip. Light is inserted from the left, reflected at the right end, and collected again at the left.

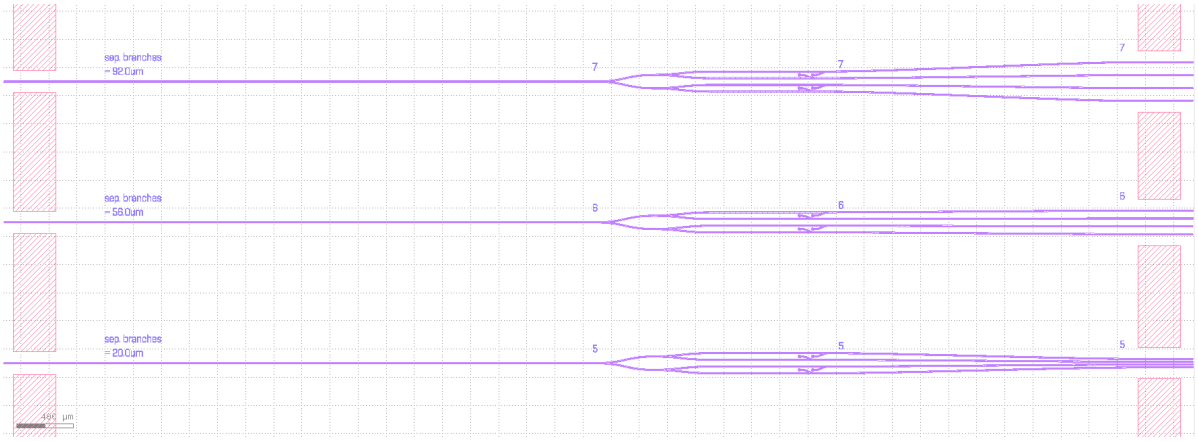

Figure B.2: Layout of three grating-coupler-based designs. A single input waveguide splits into four branches, with each design differing in the separation of the output branches to define the overall image size. The position and structure of the grating couplers, placed at two-thirds of the chip width, are identical across all designs.

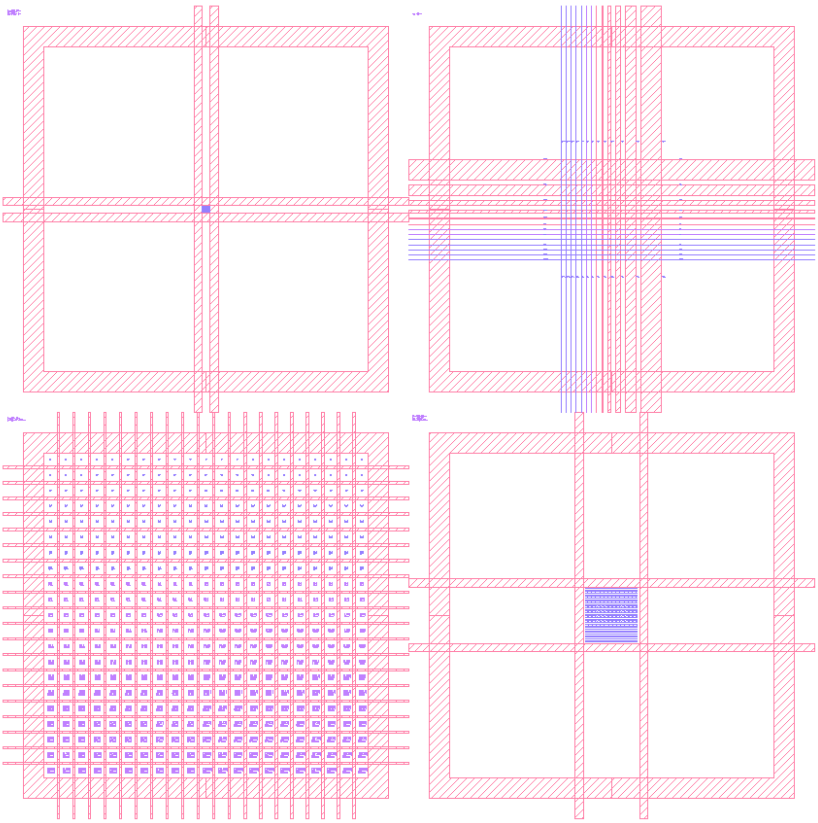

Figure B.3: Design of the image sample.

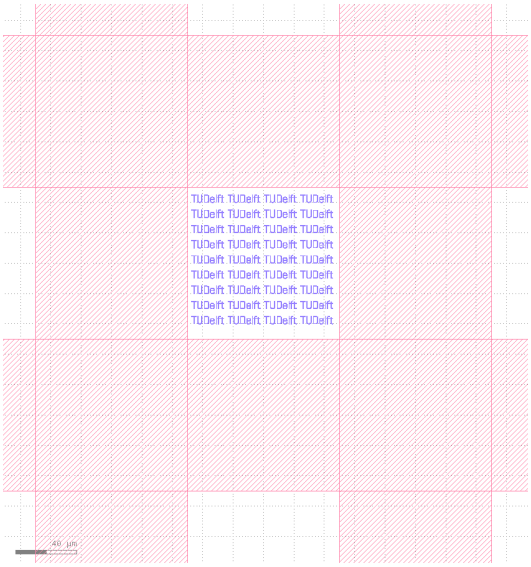

(a) Detail upper-left side

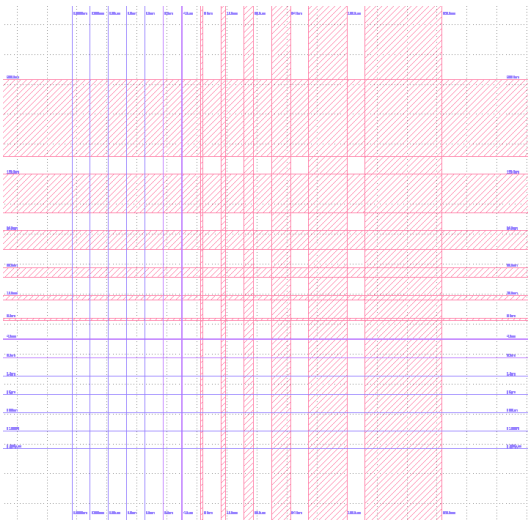

(b) Detail upper-right side

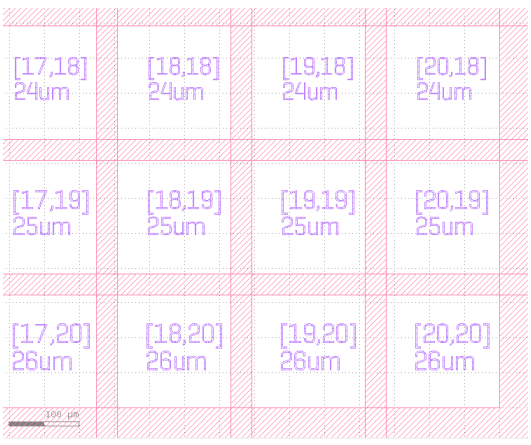

(c) Detail bottom-left side

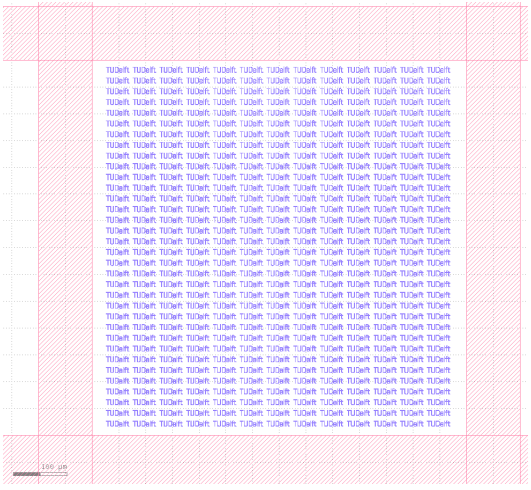

(d) Detail bottom-right side

C

Power Stability

Table C.1: *Stability measurement without an optical attenuator*

Driver Current	**Mean Measured Power**
5.00 mA	no data obtained
7.50 mA	$\mathbf{115.5 \pm 7.453}\,\mu$W
10.00 mA	$795.2 \pm 1.275\,\mu$W
15.00 mA	$2245 \pm 4.752\,\mu$W
20.00 mA	$3746 \pm 3.430\,\mu$W

Table C.2: Stability measurement with an optical attenuator

Driver Current	**Mean Output Power**
5.00 mA	no data obtained
7.50 mA	$2.282 \pm 0.166\,\mu$W
10.00 mA	$39.62 \pm 0.26\,\mu$W
15.00 mA	$\mathbf{115.4 \pm 0.747}\,\mu$W
20.00 mA	$193.9 \pm 0.977\,\mu$W

Here, a Thorlabs LDC201CU current source is used to drive a laser diode at a wavelength of 881.1 nm, in combination with a Thorlabs VOA850-FC fiber attenuator. The attenuator provides a stabilizing effect. Also, by operating the driver in a stable regime and applying attenuation afterward, the desired, stable, output laser power can be achieved.

D

Code Scanning Process

This section of the code illustrates the differences between the discrete (stepwise) and continuous scanning processes.

The discrete scanning process is described as follows:

Listing D.1: MATLAB code for motor-controlled scanning and data acquisition.

```
...
% Loop over all scanning commands
for i = 1:length(obj.command_list_x)
    index = i;

    %Ensure all motors (x,y,z) are stationary before proceeding
    motor_obj.continue_when_all_stationary('x','y','z');
    pause(0.05); % Small buffer time to guarantee stability

    %Acquire detector counts from APD (or SNSPD)
    c = get_driver_counts2(obj.APD);
    power = c(5); % Use channel 5 of the detector as measurement input

    %Store current position and measured power
    A = [x_pos_current, y_pos_current, power];
    myDataFile.write_file(A);

    %Update data matrix (image representation of scan)
    obj.dataMatrix(obj.Ny_listed(index)+1, obj.Nx_listed(index)+1) = power;
    set(obj.Image_out,'CData', obj.dataMatrix);

    %Move motor in x-direction if next command requires it
    if obj.command_list_x(index) ~= 0
        step_x = obj.command_list_x(index);
        motor_obj.move_when_stationary(step_x, 'x','z','y');
    end

    %Move motor in y-direction when stepping to next scan row
    if obj.command_list_y(index) ~= 0
        step_y = obj.command_list_y(index);
        motor_obj.move_when_stationary(step_y, 'y','z','x');
    end

    % Update current position record
    y_pos_current = y_pos_current + obj.command_list_y(index);
    x_pos_current = x_pos_current + obj.command_list_x(index);
end
...
```

The continuous scanning process, on the other hand, is described as follows:

Listing D.2: Continuous scanning routine with motorized stage and detector readout.

```
...
% Loop through all scanning commands
for i = 1:length(obj.command_list_x)
    index = i;

    % Ensure all motors (x, y, z) are stationary before starting
    motor_obj.continue_when_all_stationary('x','y','z');

    % Move in x-direction if command specifies a step
    if obj.command_list_x(index) ~= 0
        step_x = obj.command_list_x(index);
        motor_obj.move_when_stationary_cont(step_x, 'x', 'z', 'y');

        % Perform continuous measurement along x-axis
        for count = 1:obj.Nx
            % Acquire detector counts (SNSPD/APD)
            c = get_driver_counts2(obj.SNSPD);
            power = c(5); % Use channel 5 for measurement

            % Record current position and measured power
            A = [x_pos_current, y_pos_current, power];
            myDataFile.write_file(A);

            % Update data matrix for live visualization
            obj.dataMatrix(obj.Ny_listed(index)+1, obj.Nx_listed(index)+1) = power;
            set(obj.Image_out, 'CData', obj.dataMatrix);

            pause(time_dy); % Wait for motor to move to next step
        end
    end

    % Move in y-direction if command specifies a step
    if obj.command_list_y(index) ~= 0
        step_y = obj.command_list_y(index); % Corrected from command_list_z
        motor_obj.move_when_stationary_cont(step_y, 'y', 'z', 'x');
    end

    % Update current position records
    y_pos_current = y_pos_current + obj.command_list_y(index);
    x_pos_current = x_pos_current + obj.command_list_x(index);
end
...
```